



저작자표시-비영리-변경금지 2.0 대한민국

이용자는 아래의 조건을 따르는 경우에 한하여 자유롭게

- 이 저작물을 복제, 배포, 전송, 전시, 공연 및 방송할 수 있습니다.

다음과 같은 조건을 따라야 합니다:



저작자표시. 귀하는 원저작자를 표시하여야 합니다.



비영리. 귀하는 이 저작물을 영리 목적으로 이용할 수 없습니다.



변경금지. 귀하는 이 저작물을 개작, 변형 또는 가공할 수 없습니다.

- 귀하는, 이 저작물의 재이용이나 배포의 경우, 이 저작물에 적용된 이용허락조건을 명확하게 나타내어야 합니다.
- 저작권자로부터 별도의 허가를 받으면 이러한 조건들은 적용되지 않습니다.

저작권법에 따른 이용자의 권리는 위의 내용에 의하여 영향을 받지 않습니다.

이것은 [이용허락규약\(Legal Code\)](#)을 이해하기 쉽게 요약한 것입니다.

[Disclaimer](#)

2013年 2月

碩士學位 論文

Hydroxyapatite Film Coating on the Nanotubular Ti-25Nb-xZr Alloys by Electrochemical deposition method

朝鮮大學校 大學院

尖端部品素材工學科

吳 沼 旻

Hydroxyapatite Film Coating on the Nanotubular Ti-25Nb-xZr Alloys by Electrochemical deposition method

나노튜브로 형성된 Ti-25Nb-xZr 합금의 전기화학적
증착법에 의한 하이드록시아파타이트 코팅

2013年 2月 25日

朝鮮大學校 大學院

尖端部品素材工學科

吳 沼 旻

Hydroxyapatite Film Coating on the Nanotubular Ti-25Nb-xZr Alloys by Electrochemical deposition method

指導教授 李 炫 珪

이 論文을 工學 碩士學位申請 論文으로 提出함

2012年 10月

朝鮮大學校 大學院

尖端部品素材工學科

吳 沼 旻

吳沼旻의 碩士學位論文을 認准함

委 員 張 朝鮮大學校 教 授 朴 珍 成 印

委 員 朝鮮大學校 助 教 授 姜 賢 喆 印

委 員 朝鮮大學校 教 授 李 炫 珪 印

2012年 11月

朝鮮大學校 大學院

CONTENTS

LIST OF TABLES	III
LIST OF FIGURES	IV
국문초록	VI

I . INTRODUCTION	1
II . BACKGROUND	3
2.1. Historical background	3
2.2. Characteristic of titanium and titanium alloys	5
2.2.1. Alpha alloys	6
2.2.2. Alpha + beta alloys	6
2.2.3. Beta alloys	6
2.3. Properties of titanium and titanium alloys	9
2.4. Titanium dioxide (TiO ₂)	11
2.4.1. TiO ₂ growth mechanism	12
2.5. Surface modification of titanium and titanium alloys	15
2.6. Calcium phosphates properties	17
2.6.1. Dihydrate calcium phosphate (DCP)	17
2.6.2. Anhydrous calcium phosphate (ADCP)	18
2.6.3. Octacalcium phosphate (OCP)	19
2.6.4. Tricalcium phosphate (TCP)	19
2.6.5. Hydroxyapatite (HA)	20
2.7. Calcium phosphate coating	22
2.8. Surface wettability	24

III . MATERIALS AND METHODS	26
3.1. Alloy preparation	26
3.2. Phase analysis of Ti-25Nb-xZr alloys	27
3.3. Nanotube formation on Ti-25Nb-xZr alloys	28
3.4. HA coating of nanotube formed on Ti-25Nb-xZr alloys by electrochemical deposition method	29
3.5. Corrosion test for Ti-25Nb-xZr alloys	31
IV . RESULTS AND DISCUSSION	32
4.1. Microstructures and XRD analysis of Ti-25Nb-xZr alloys	32
4.2. The nanotube formed of Ti-25Nb-xZr alloys	35
4.3. Electrochemical characteristics of Ti-25Nb-xZr alloys with surface treatment	40
4.4. HA coating of nanotube formed on Ti-25Nb-xZr alloys	43
4.5. Surface wettability test of Ti-25Nb-xZr alloys	46
V . CONCLUSIONS	48
- REFERENCES -	50

LIST OF TABLES

Table 1. Physical properties of titanium	4
Table 2. Introduction year and maximum working temperature for some titanium alloys	4
Table 3. Common alloying elements and their stabilizing effect	8
Table 4. Surface modification methods for titanium and its alloys implants	16
Table 5. The calcium phosphate phases used to date for coatings in orthopaedic devices	17
Table 6. Typical compositional values of inorganic phase of adult human calcified tissues	21
Table 7. Different technique to deposit HA coatings	23
Table 8. The conditions of nanotube formation on Ti-25Nb-xZr alloys	28
Table 9. The condition of electrochemical deposition on nanotubular Ti-25Nb-xZr alloys	30
Table 10. The conditions of electrochemical corrosion test on Ti-25Nb-xZr alloys	31
Table 11. Electrochemical parameter of non-treated and nanotube formed Ti-25Nb-xZr alloys from polarization curves: Corrosion current density (I_{corr}), current density at 300mV (I_{300mV}), corrosion current potential (E_{corr}) and passivation current density (I_{pass})	42

LIST OF FIGURES

Fig. 1. Allotropic transformation of titanium	7
Fig. 2. Effect of interstitial alloying elements on strength and reduction in area of titanium. The shaded area is for reduction in area values, when nitrogen, carbon or oxygen is present	7
Fig. 3. Compositions of U.S. technical alloys mapped onto a pseudobinary β -isomorphous phase diagram	8
Fig. 4. Bulk structure of rutile and anatase. The stacking of the octahedral in both structure are shown on the right side	14
Fig. 5. This schematic illustrates the electrochemical anodization process used to fabricate the titanium oxide (TiO_2) nanotube surface on titanium (Ti) metal	14
Fig. 6. This schematic illustration of a contact angle formed by a liquid drop at the solid/liquid interface and the liquid/vapor interface	25
Fig. 7. This schematic illustration of (a) a hydrophobic or non-wetting surface and (b) hydrophilic or wetting surface	25
Fig. 8. Process of monitoring voltage versus times during the formation of HA deposition	29
Fig. 9. OM images of Ti-25Nb-xZr alloys (a) Ti-25Nb-3Zr, (b) Ti-25Nb-7Zr and (c) Ti-25Nb-15Zr	33
Fig. 10. FE-SEM images of Ti-25Nb-xZr alloys (a) Ti-25Nb-3Zr, (b) Ti-25Nb-7Zr and (c) Ti-25Nb-15Zr	33
Fig. 11. XRD patterns of Ti-25Nb-xZr alloys (a) Ti-25Nb-3Zr, (b) Ti-25Nb-7Zr and (c) Ti-25Nb-15Zr	34
Fig. 12. FE-SEM images of nanotube formed on Ti-25Nb-xZr alloys:	

top view, cross-section and bottom view (a) Ti-25Nb-3Zr, (b) Ti-25Nb-7Zr and (c) Ti-25Nb-15Zr	37
Fig. 13. Bright-field STEM images, diffraction patterns, and EDS peaks for cross-sectioned nanotube surfaces on Ti-25Nb-15Zr alloy	38
Fig. 14. XRD patterns of nanotube formed on Ti-25Nb-xZr alloys (a) Ti-25Nb-3Zr, (b) Ti-25Nb-7Zr and (c) Ti-25Nb-15Zr	39
Fig. 15. Polarization curve of Ti-25Nb-xZr alloys after potentiodynamic test in 0.9 % NaCl solution at 36.5 ± 1 °C	41
Fig. 16. Polarization curve of nanotube formed on Ti-25Nb-xZr alloys after potentiodynamic test in 0.9 % NaCl solution at 36.5 ± 1 °C	41
Fig. 17. FE-SEM micrographs of Hydroxyapatite coating by 2.5 mM $\text{Ca}(\text{NO}_3)_2$ + 1.5 mM $\text{NH}_4\text{H}_2\text{PO}_4$ electrolyte with 5, 10, 30 cycles of potential on nanotube formed Ti-25Nb-15Zr alloy(a, a-1 and a-2) and 5.0 mM $\text{Ca}(\text{NO}_3)_2$ + 3.0 mM $\text{NH}_4\text{H}_2\text{PO}_4$ electrolyte with 5, 10, 30 cycles of potential on nanotube formed Ti-25Nb-15Zr alloy(b, b-1 and b-2)	44
Fig. 18. XRD patterns of Hydroxyapatite coating on nanotube formed Ti-25Nb-15Zr alloy (a) 2.5 mM Ca-P solution (b) 5.0 mM Ca-P solution	45
Fig. 19. Snap shot of contact angles on the different surface treatment (a) non-treated alloys (b) nanotube formed alloys (c) 2.5 mM Ca-P solution alloys and (d) 5.0 mM Ca-P solution alloys	47
Fig. 20. Contact angles values of water droplets measured on the different surface treatment	47

국 문 초 록

나노튜브로 형성된 Ti-25Nb-xZr 합금의 전기화학적 증착법에 의한 하이드록시아파타이트 코팅

오 소 민

지도교수: 이현규, 공학박사

첨단부품소재공학과

조선대학교 대학원

본 논문에서는 양극산화법을 이용하여 나노튜브를 형성하고, 그 표면에 전기화학적 증착법을 이용하여 하이드록시아파타이트를 코팅한 Ti-25Nb-xZr 삼원계 합금의 표면특성을 연구하였다. 이 삼원계 합금은 Ti-25Nb 이원계 합금을 기본으로 하여 Zr 함량을 3, 7 및 15 wt.%로 칭량해 합금을 설계하였다. 설계된 합금은 아크 용해로에서 균일하게 용해를 한 뒤 1000 °C에서 24시간동안 열처리한 후 급냉하여 3 mm 두께의 디스크형태로 시편을 제조하였다. 1.0 M H₃PO₄ 용액에 0.8 wt.% NaF를 첨가한 전해질 용액으로 양극산화법을 통해 표면에 나노튜브를 형성하였고, 나노튜브를 형성한 후 전기화학적 증착법을 이용하여 하이드록시아파타이트를 코팅하였다.

모든 시험편의 표면은 OM, XRD, FE-SEM, EDS 및 TEM 등으로 분석하였으며 표면의 전기화학적 부식 거동은 동전위 분극시험을 통해 분석하였고, 나노튜브와 하이드록시아파타이트가 코팅된 Ti-25Nb-xZr 합금의 표면을 접촉각 측정으로 젖음성을 평가하였고 다음과 같은 결과를 얻었다.

1. Ti-25Nb-xZr 합금은 등축정에 근접한 구조로 Zr 함량이 증가할수록 침상조직에서 등축정과 약간의 침상조직이 혼합된 형태가 관찰되었다. X선 회절분석 결과를 통해 합금의 Zr 함량이 증가할수록 $\alpha'' + \beta$ 상에서 점점 β 상으로 변하였다.

2. 양극산화법을 이용해 나노튜브를 형성한 후 anatase 와 rutile 의 TiO_2 상의 X선 회절분석 결과가 나타났으며, 나노튜브의 크기가 다른 2개의 구조를 보였다. 큰 튜브는 직경이 대략 180 ~ 220 nm, 작은 튜브의 직경은 대략 80 ~ 110 nm 였고, Zr 함량이 증가할수록 튜브의 길이 또한 증가하였으며, 규칙적인 형태의 튜브 구조를 보였다.
3. 동전위 분극시험을 시행한 뒤 분극곡선을 통해 Ti-25Nb-xZr 합금은 Zr 함량이 증가함에 따라 우수한 내식성을 나타내었고, 이는 Zr이 높은 전위에서도 Ti와 같이 화학적으로 안정하여 쉽게 용출되지 않고, ZrO_2 산화피막을 형성하여 내식성을 향상시키는 것으로 생각된다.
4. 접촉각 측정의 결과로부터, 양극산화법을 이용해 나노튜브를 형성한 후 전기 화학적 증착법을 이용해 하이드록시아파타이트를 코팅한 Ti-25Nb-xZr 합금이 가장 우수한 젖음성을 나타내었다.
5. 전기화학적 증착법을 이용한 하이드록시아파타이트 코팅에서 전해질의 농도 차이에 의해 칼슘포스페이트의 형상이 다른것으로 관찰된다. 낮은 전해질 농도인 2.5 mM에서는 나노튜브에 의해 형성된 튜브표면에 부분적으로 칼슘포스페이트가 형성되는 것을 관찰할 수 있었으며, 5.0 mM에서는 나노튜브 포어를 관찰할 수 없었다.

결론적으로, 전기화학적 증착법을 이용하여 하이드록시아파타이트를 코팅한 결과, 전해질의 농도에 따라 칼슘포스페이트의 크기를 제어할수 있으며, 나노튜브 기공내부까지도 형성되어 생체적합성이 향상되는 것을 확인할 수 있었다.

I . INTRODUCTION

The average age and life expectancy of human beings has continuously increased since 1950, and the increasing trend is predicted to accelerate in the future. This leads to the ever-increasing demand for biomedical implant materials in our times and the future [1]. Metallic biomaterials such as stainless steels, Co-based alloys, Commercially pure titanium and Ti-6Al-4V alloys have been extensively used in the medical applications. Also the titanium and its alloys are widely used as implants in orthopedics, dentistry and cardiology due to their outstanding properties such as high strength, enhanced biocompatibility, relatively good fatigue resistance and superior corrosion capacity [2,3]. Among the various types of Ti alloys, Ti-6Al-4V alloy has been the choice in many instances.

However the two major concerns are: the leaching of V and Al that could cause long term health problems such as peripheral neuropathy, osteomalacia and Alzheimer diseases [4]; and the large modulus mismatch between the Ti-6Al-4V alloy (~110Gpa) and the bone (~10-40Gpa), which could cause insufficient loading on bone adjacent to the implant, leading to an eventual failure of the implant [5]. These concerns have led to the development of new type titanium alloys without aluminium and vanadium. It has been reported that, β rich Ti-Nb-Zr alloys are better substitutes, as these materials possess low modulus and consists of non-toxic elements in it [6]. The Nb present in these alloys, a known β stabilizer reduces the modulus of the alloy. Further, the presence of β phase in the microstructure enhances the ability of the alloys to harden on subsequent aging. The addition of Zr results in high level of blood compatibility when used in cardiovascular implants and leads to better corrosion resistance due to the formation of stable oxide layer [7].

Calcium phosphate(Ca-P) bioceramics and in particular hydroxyapatite [HA, $\text{Ca}_{10}(\text{PO}_4)_6(\text{OH})_2$] are an important class of biomaterials that have received considerable attention as coating for orthopaedic and dental implants due to their osteoconductive properties [8] and their ability to act as a protective layer to prevent the leaching of undesirable metal ions into the

surrounding environment [9].

Anodic oxidation is commonly used for surface treatment of metals, especially to obtain microporous structure at the surfaces. It is found that by anodic oxidation the regular arrays of oxide nanotubes can grow on many metals such as zirconium, niobium, tantalum, hafnium and titanium [10]. The titania nanotube layer is attractive due to its excellent properties in optics, electronics, photochemistry, and biology [11].

More recently, the addition of titanium dioxide(TiO_2) into Ca-P coating in order to create composite surfaces has been recognized as a key route for enhancing their stability and providing the appropriate biofunctionality [12,13]. In the past decade, several methods have been reported to deposit HA onto implant surfaces, for example, plasma spray, RF sputtering, pulsed laser-deposition, sol-gel, and electrochemical deposition, etc [14,15].

Electrochemical deposition has currently attracted the commercial method for coating on titanium implant surfaces, which is an attractive process because highly irregular objects can be coated relatively quickly at low temperatures. Additionally, the thickness and chemical composition of coatings can be well controlled through adequate conditions of the process [16].

Hence, in this study, we investigated the hydroxyapatite film coating on the nanotubular Ti-25Nb-xZr alloys by electrochemical deposition method.

II . BACKGROUND

2.1. Historical background

Titanium is widely distributed in the universe. It is abundant on Earth and has been detected in meteorites, the moon, the sun and other stars. Its concentration within the earth's crust of about 0.6 % makes it the fourth most abundant of the metals after aluminium, iron and magnesium. There are 20 times more in quantity than chromium, 30 times more than nickel, 60 times more than copper, 100 times more than tungsten and 600 times more than molybdenum [17]. Some of the physical properties of titanium are listed in Table 1 [18].

The Titanium Metals Company of America (TMCA) produced the first commercial products around 1950 [19]. Since then, the production of the metal has grown at an average annual rate of about 8 %, and over the past 50 years, titanium and its alloys have proven to be technically superior and cost-effective materials for structures. More specifically, a wide variety of aerospace, marine and other industrial applications is now commercially viable due to their superb combined properties, when compared with other metallic materials. Some of the developments in titanium alloys over this period are summarised in Table 2 [20,21]. As can be seen, the most common titanium alloy used today, Ti-6Al-4V, was introduced in the mid-1950s with a maximum working temperature of 300 ° C. The highest temperature that a titanium alloy can be used today lies just below 600 ° C. By implementing adequate cooling design, coating processing or thermochemical treatment, the maximum working temperature of titanium alloys can be increased.

Table 1. Physical properties of titanium [18]

Property	Atomic number	Atomic weight	Density	Transformation temperature	Crystal structure		
					Alpha, HCP		Beta, BCC
					c	a	a
Value	22	47.9 g/mol	4.54 g/cm ³	882.5 °C	4.6832 Å	2.9504 Å	3.28 Å

Table 2. Introduction year and maximum working temperature for some titanium alloys [20,21]

Alloy	Composition (wt. %)	Introduction year	Max working temperature (°C)
Ti-64	6Al, 4V	1954	300
IMI-550	4Al, 2Sn, 4Mo, 0.5Si	1956	425
Ti-811	8Al, 1Mo, 1V	1961	400
IMI-679	2Al, 11Sn, 5Zr, 1Mo, 0.2Si	1961	450
Ti-6246	6Al, 2Sn, 4Zr, 6Mo	1966	450
Ti-6242	6Al, 2Sn, 4Zr, 2Mo	1967	450
IMI-685	6Al, 5Zr, 0.5Mo, 0.25Si	1969	520
Ti-11	6Al, 2Sn, 1.5Zr, 1Mo, 0.1Si, 0.3Bi	1972	540
Ti-17	5Al, 2Sn, 2Zr, 4Mo, 4Cr	1973	350
Ti-6242S	6Al, 2Sn, 4Zr, 2Mo, 0.1Si	1974	520
IMI-829	5.5Al, 3.5Sn, 3Zr, 0.3Mo, 1Nb, 0.3Si	1976	580
IMI-834	5.5Al, 4Sn, 4Zr, 0.3Mo, 1Nb, 0.5Si, 0.06C	1984	590

2.2. Characteristic of titanium and titanium alloys

Titanium exists in two crystallographic forms. At room temperature, pure titanium has a hexagonal close-packed (hcp) crystal structure referred to as α -phase. At 882.5 ° C, this transforms to a body-centered cubic (bcc) structure known as β -phase (Fig. 1). The manipulation of these crystallographic variations through alloying additions and thermochemical processing is the basis for the development of a wide range of alloys and properties [22,23].

The alloying elements have different influences on the properties of titanium. For example, aluminium, vanadium, iron, chromium, tin and silicon increase the value of the tensile yield strength and ultimate tensile strength. At the same time, they decrease the ductility and the toughness. Aluminium, zirconium and molybdenum increase the heat resistance, while the corrosion resistance can be increased by molybdenum, zirconium, niobium, tantalum and palladium. Some of the most common alloying elements and their stabilizing effect are shown in Table 3 [21,24].

On the other hand, elements such as nitrogen, carbon and especially oxygen have a strong α -stabilizing effect and thereby raise the $\alpha \rightarrow \beta$ transition temperature (β -transus), whereas hydrogen, which has a β -stabilizing effect, lowers the transus temperature. Increasing the amount of interstitial elements leads to a drastic increase in strength (Fig. 2), but at the same time, leads to a sharp drop in ductility and with an increased risk of embrittlement [25]. Based on the phases present, titanium alloys can be classified as α alloys, β alloys or $\alpha + \beta$ alloys. Within the last category are the subclasses near- α and near- β , referring to alloys with compositions which place them near to $\alpha / (\alpha + \beta)$ or $(\alpha + \beta) / \beta$ -phase boundaries, respectively.

The most commonly used titanium alloys are presented in phase-diagram format, Fig. 3 [29], to show the interactions between the alloy's α - and β -stabilizing components.

2.2.1 Alpha alloys

Alpha alloys contain elements such as aluminium and tin. These α -stabilizing elements increase the phase transformation temperature. They are characterized by satisfactory strength, toughness and weldability but poorer forgeability than β alloys. The absence of a ductile-brittle transformation, a property of the bcc structure, makes α alloys suitable for cryogenic applications [26].

2.2.2 Alpha + beta alloys

Alpha + beta alloys have a composition that supports a mixture of α and β phases. Although many binary β -stabilized alloys in thermodynamic equilibrium are two phase, in practice, the $\alpha+\beta$ alloys usually contain mixtures of both α and β stabilizers. The properties of these alloys can be controlled through heat treatment, which is used to adjust the amounts and types of phases present [27]. Alpha + beta alloys generally exhibit good fabricability as well as high room temperature strength and moderate elevated-temperature strength. The most commonly used $\alpha+\beta$ alloy is Ti-6Al-4V.

2.2.3 Beta alloys

Beta alloys contain elements such as vanadium, molybdenum, iron and chromium, which decrease the temperature of the α to β phase transition. There are several commercial β alloys such as Ti-10V-2Fe-3Al, Ti-15V-3Cr-3Al-2Sn and Ti-3Al-8V-6Cr-4Mo-4Zr. Beta alloys, according to Ref. [28], are extremely formable. They are also prone to ductile-brittle transformation, and along with other bcc-phase alloys, are unsuitable for low-temperature application.

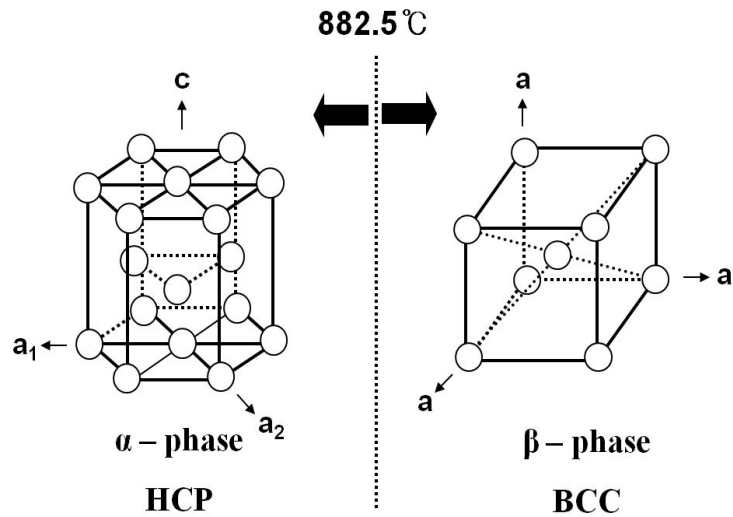


Fig. 1. Allotropic transformation of titanium [22,23].

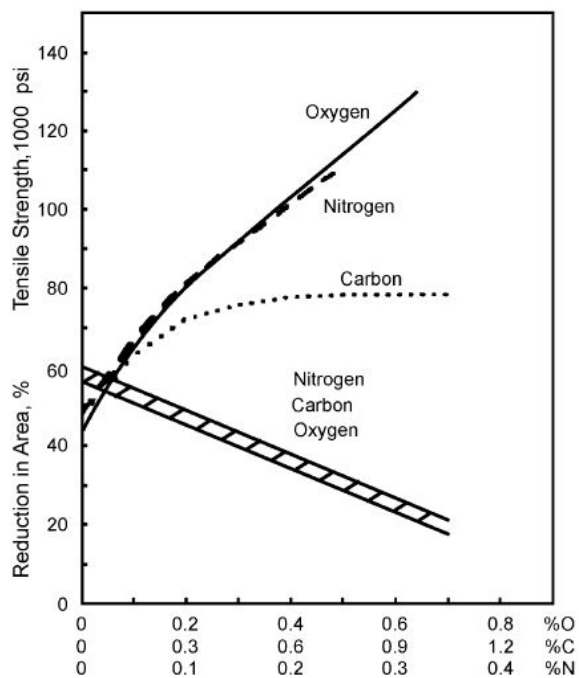


Fig. 2. Effect of interstitial alloying elements on strength and reduction in area of titanium [25]. The shaded area is for reduction in area values, when nitrogen, carbon or oxygen is present.

Table 3. Common alloying elements and their stabilizing effect [21,24]

Alloying element	Range (wt.%)	Effect on structure
Aluminium	2 to 7	α -stabilizer
Tin	2 to 6	α -stabilizer
Vanadium	2 to 20	β -stabilizer
Molybdenum	2 to 20	β -stabilizer
Chromium	2 to 12	β -stabilizer
Copper	2 to 6	β -stabilizer
Zirconium	2 to 8	α and β strengthening
Silicon	0.2 to 1	Improves creep resistance

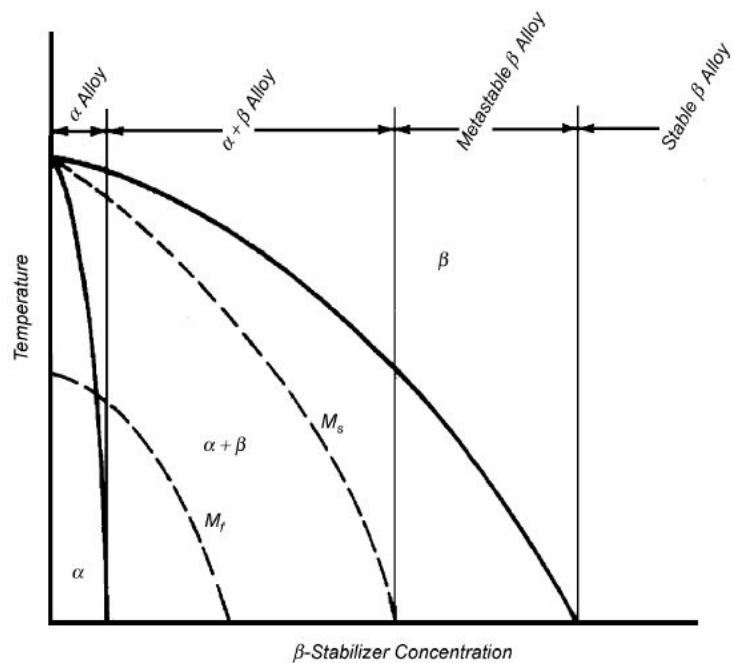


Fig. 3. Compositions of U.S. technical alloys mapped onto a pseudobinary β -isomorphous phase diagram [29].

2.3. Properties of titanium and titanium alloys

Titanium and titanium alloys have some very attractive properties enabling them to be used in many industries. Some of their advantages are: excellent corrosion and erosion resistance; low densities, which give high specific strength-to-weight ratios allowing lighter and stronger structures; high-temperature capability and in some cases, cryogenic properties. They are widely used in aerospace applications, marine applications, many corrosive environments, sports equipment and medicine [30]. Titanium is completely neutral to the human body and is frequently used in the medical field to replace heart valves, joints and bones. Titanium replacements for hips and other joints are well established and have been in use for over 30 years. The biocompatibility and strength of titanium make it an ideal material for dental posts and other oral prosthetics. Bone naturally adheres to the surface oxide of titanium without additional coatings [31].

Hydroxyapatite coatings on titanium implants are becoming very popular because of enhancing the biocompatibility and the life of the implants. They also allow direct bonding between bone and implant and accelerate the process of healing and growth of the bone [32]. Titanium golf shafts, tennis racquet frames, pool cue shafts and bicycle frames are currently being fabricated using alloys such as Ti-3Al-2.5V. They have the properties needed for sports applications like low modulus of elasticity, damage tolerance, good strength-to-weight ratios and good corrosion resistance. At the same time, titanium and titanium alloys have found little use in mechanical engineering applications because of their poor tribological properties such as poor abrasive wear resistance, poor fretting behaviour and high coefficient of friction. The poor fretting behaviour can be improved by applying different surface treatments and coatings [33].

According to Ref. [33], there are four main mechanisms that can be used for such improvement: (i) to induce a compressive residual stress; (ii) to decrease the coefficient of friction; (iii) to increase the hardness; and

(iv) to increase the surface roughness. The friction problem is related to the crystal structure and reactivity of titanium and can be largely overcome by changing the nature of the surface using such surface engineering technologies as different thermochemical treatments, so that the surface is no longer titanium, but a hard compound of titanium. In order to improve such mechanical properties, surface thermochemical treatments can be applied.

2.4. Titanium dioxide (TiO₂)

Titanium oxide is known to have varying stoichiometries and the common compounds are Ti₃O to Ti₂O, Ti₃O₂, TiO, Ti₂O₃, Ti₃O₅ and TiO₂. This is a consequence of the facts that titanium exists in many different stable oxidation states and that oxygen is highly soluble in titanium. The most stable titanium oxide is TiO₂, with titanium in the preferred oxidation state of +IV. Titanium oxides, in particular TiO₂, are thermodynamically very stable and the Gibbs free energy of formation is highly negative for a variety of oxidation media, such as water or oxygen containing organic molecules [34].

TiO₂ exists in three different crystallographic forms: rutile, anatase with tetragonal and brookite with orthorhombic structure, but only the rutile and anatase phases are practically important. The unit cells of rutile and anatase are shown in Fig. 4 [35]. In both structure, the basic building block consists of a titanium atom surrounded by six oxygen atoms in a more or less distorted octahedral configuration. The two bonds between titanium and oxygen at the apices of the octahedron are slightly longer. A sizable deviation from a 90° bond angle is observed in anatase. In the rutile structure, neighboring octahedrals share one corner along the <100> plane and are stacked with their long axis alternating by 90°.

The mechanism of TiO₂ nanotube formation in fluoride-based electrolytes is said to occur as a result of three simultaneous processes: (i) the field assisted oxidation of Ti metal to form titanium dioxide; (ii) the field assisted dissolution of Ti metal ions in the electrolyte; and (iii) the chemical dissolution of Ti and TiO₂ due to etching by fluoride ions [36].

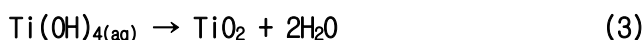
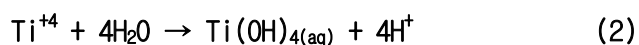
TiO₂ nanotubes are not formed on the pure Ti surface but on the thin TiO₂ oxide layer naturally present on the Ti surface. The two-electrode electrochemical anodization set-up is schematically shown in Fig 5. A Ti sheet is used as the anode and a platinum (Pt) sheet is used as the cathode submersed in a fluoride-based electrolyte solution. The duration and

magnitude of power supplied to the system determines the height and diameter of the nanotubes.

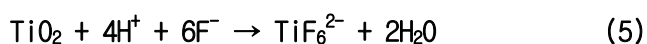
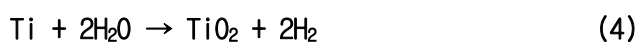
2.4.1 TiO₂ growth mechanism

The growth mechanisms of array TiO₂ mainly consist of chemical dissolution and electrochemical oxidation. The chemical dissolution process controls the formation structures and the geometric sizes of the TiO₂ nanotubes. The anodization voltage, anodization time, and acid concentration are critical parameters for electrochemical oxidation.

In the growth mechanism of array TiO₂ nanotubes, the ammonium fluoride in the solution firstly dissociates into ammonia and hydrofluoric acid. The titanium foil at the anode then dissolves with the electrolysis of water. Ti⁴⁺ ions (see Eq. (1)) ejected from the anode migrate through the oxide under the application of an electric field and accumulate at the entrances of the nanopores. The electrolysis of water releases O₂ due to the interaction of Ti metal with O²⁻ or OH⁻ ions [37]. The F⁻, O²⁻, and OH⁻ species move toward the anode and the Ti⁴⁺ ions move toward the electrolyte. Then, Ti(OH)₄ precipitate (see Eq. (2)) forms via the instantaneous hydrolysis reaction at the entrances of the nanopores. These anions migrate through the oxide layer to the Ti metal/oxide interface and react with the Ti metal. Bowl-like pores initially form on the Ti foil surface due to the pitting corrosion of F⁻ ions. At the same time, the TiO₂ dissolution in the presence of fluoride also occurs corresponding to the chemical etching, and hydrogen fluoride is consumed. The chemical reaction is as follows:



The TiO₂ nanotubes are described as the formation of the anodic layer under an applied electric field (see Eq. (4)) and as the chemical field assisted dissolution of the forming oxide (see Eq. (5)). Fluoride ions dissolve the TiO₂ forming a complex compound. The TiO₂ at the bottom of the bowl-like pores combines with F⁻ ions and then dissolves into the electrolyte in the form of soluble. The oxidation rate is limited by the thickness of the barrier layer at the Ti metal/oxide interface and is kept active by the chemical dissolution process at the oxide/electrolyte interface.



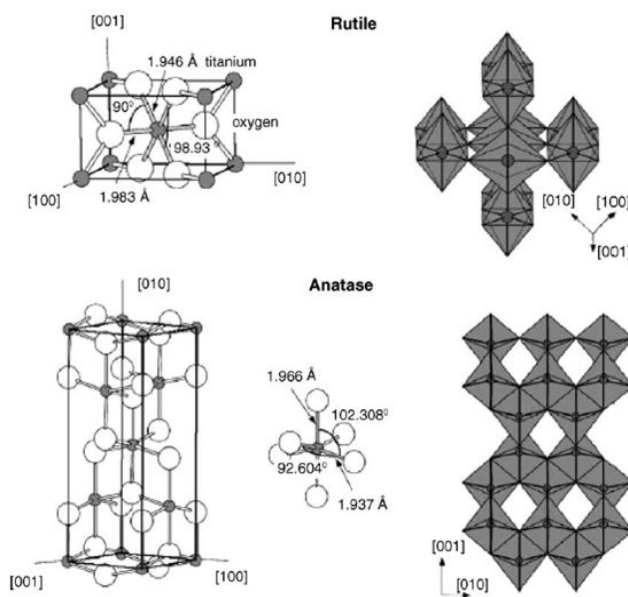


Fig. 4. Bulk structure of rutile and anatase. The stacking of the octahedral in both structure are shown on the right side [35].

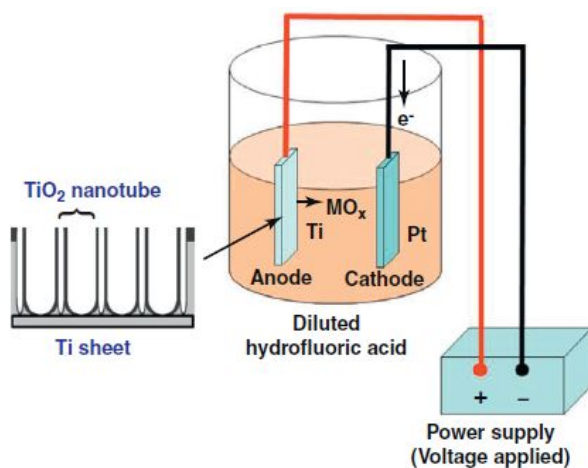


Fig. 5. This schematic illustrates the electrochemical anodization process used to fabricate the titanium oxide (TiO₂) nanotube surface on titanium (Ti) metal.

2.5. Surface modification of titanium and titanium alloys

The bulk properties of biomaterials, such as non-toxicity, corrosion resistance or controlled degradability, modulus of elasticity, and fatigue strength have long been recognized to be highly relevant in terms of the selection of the right biomaterials for a specific biomedical application. The events after implantation include interactions between the biological environment and artificial material surfaces, onset of biological reactions, as well as the particular response paths chosen by the body.

The material surface plays an extremely important role in the response of the biological environment to the artificial medical devices. In implants made of titanium, the normal manufacturing steps usually lead to an oxidized, contaminated surface layer that is often stressed and plastically deformed, non-uniform and rather poorly defined. Such "native" surfaces are clearly not appropriate for biomedical applications and some surface treatment must be performed. Another important reason for conducting surface modification to titanium medical devices is that specific surface properties that are different from those in the bulk are often required. For example, in order to accomplish biological integration, it is necessary to have good bone formability. In blood-contacting devices, such as artificial heart valves, blood compatibility is crucial. In other applications, good wear and corrosion resistance is also required.

The proper surface modification techniques not only retain the excellent bulk attributes of titanium and its alloys, such as relatively low modulus, good fatigue strength, formability and machinability, but also improve specific surface properties required by different clinical applications. According to the different clinical needs, various surface modification schemes have been proposed and are shown in Table 4 [38].

In the following sections, the improvement of biocompatibility, wear and corrosion resistance, bioactivity, blood compatibility of titanium and titanium alloys using various surface modification technologies are

discussed. These methods are classified into mechanical, chemical and physical methods according to the formation mechanism of the modified layer on the material surface.

Table 4. Surface modification methods for titanium and its alloys implants [38]

Surface modification methods	Modified layer	Objective
Mechanical methods		
Machining	Rough or smooth surface formed by subtraction process	Produce specific surface topographies; clean and roughen surface; improve adhesion in bonding
Grinding		
Polishing		
Blasting		
Chemical methods		
Chemical treatment		
Acidic treatment	<10 nm of surface oxide layer	Remove oxide scales and contamination
Alkaline treatment	~1 μm of sodium titanate gel	Improve biocompatibility, bioactivity or bone conductivity
Hydrogen peroxide treatment	~5 nm of dense inner oxide and porous outer layer	Improving biocompatibility, bioactivity or bone conductivity
Sol-gel	~10 μm of thin film, such as calcium phosphate, TiO_2 and silica	Improve biocompatibility, bioactivity or bone conductivity
Anodic oxidation	~10 nm to 40 μm of TiO_2 layer, adsorption and incorporation of electrolyte anions	Produce specific surface topographies; improved corrosion resistance; improve biocompatibility, bioactivity or bone conductivity
CVD	~1 μm of TiN, TiC, TiCN, diamond and diamond-like carbon thin film	Improve wear resistance, corrosion resistance and blood compatibility
Biochemical methods	Modification through silanized titania, photochemistry, self-assembled monolayers, protein-resistance, etc.	Induce specific cell and tissue response by means of surface-immobilized peptides, proteins, or growth factors
Physical methods		
Thermal spray		
Flame spray	~30 to ~200 μm of coatings, such as titanium, HA, calcium silicate, Al_2O_3 , ZrO_2 , TiO_2	Improve wear resistance, corrosion resistance and biological properties
Plasma spray		
HVOF		
DGUN		
PVD		
Evaporation	~1 μm of TiN, TiC, TiCN, diamond and diamond-like carbon thin film	Improve wear resistance, corrosion resistance and blood compatibility
Ion plating		
Sputtering		
Ion implantation and deposition		
Beam-line ion implantation	~10 nm of surface modified layer and/or ~ μm of thin film	Modify surface composition; improve wear, corrosion resistance, and biocompatibility
PIII		
Glow discharge plasma treatment	~1 nm to ~100 nm of surface modified layer	Clean, sterilize, oxide, nitride surface; remove native oxide layer

2.6. Calcium phosphates properties

Biologically relevant calcium phosphate (CaP) belong to the orthophosphate group and naturally occur in several biological structures, including teeth and bone. Bone consists of an inorganic component of biological apatites (CaP) and an organic component, consisting primarily of collagen and water. Synthetic hydroxyapatite has been demonstrated to have very similar properties to the naturally occurring CaP of the inorganic component of bone. Consequently, CaP have long been investigated and utilized as coatings for protection against wear corrosion and increased biocompatibility in orthopaedic devices. Table 5 summarizes the calcium phosphate phases, and a brief review of their properties follows below.

Table 5. The calcium phosphate phases used to date for coatings in orthopaedic devices

Name	Formula	Ca/P ratio
Calcium phosphate dihydrate (brushite)	$\text{CaHPO}_4 \cdot 2\text{H}_2\text{O}$	1.0
Anhydrous calcium phosphate (monetite)	CaHPO_4	1.0
Octacalcium phosphate	$\text{Ca}_8\text{H}_2(\text{PO}_4)_6 \cdot 5\text{H}_2\text{O}$	1.33
Tricalcium phosphate (whitlockite)	$\text{Ca}_3(\text{PO}_4)_2$	1.5
Fluorapatite	$\text{Ca}_{10}(\text{PO}_4)_6\text{F}_2$	1.67
Hydroxyapatite	$\text{Ca}_{10}(\text{PO}_4)_6(\text{OH})_2$	1.67

2.6.1 Dihydrate calcium phosphate - brushite (DCP)

DCP crystals are monoclinic and exhibit greater solubility than most other calcium phosphate phases. Whilst DCP demonstrates greater solubility

compared to the other calcium phosphate phases mentioned in Table 5, it is a precursor to the more stable phase hydroxyapatite. For this reason, several studies have focused on the use of DCP coatings as an initial step to obtaining HA. The synthesis of HA through precipitation techniques often results in the formation of tightly packed small crystals. However, this crystal size is often difficult to control. It is therefore advantageous to use of DCP as a precursor, as it is possible to modify the crystal size of DCP through homogeneous precipitation, which can then be converted directly to HA. In environments with a pH greater than 6-7, brushite becomes unstable and transforms to the more favourable HA phase. Prior investigations have also utilized the increased solubility of DCP on metallic implants as a means of increasing the amounts of calcium and phosphate ions available in the immediate vicinity of the implant to promote increased osseointegration. DCP is also often used as the preliminary component of bone cements in the clinical field. Previous in vitro studies have shown DCP to be a promising coating for clinical use. Its biocompatibility has been demonstrated with several cell lines, including pre-osteoblastic murine macrophage cells and murine fibroblastic cells.

2.6.2 Anhydrous calcium phosphate - monetite (ADCP)

ADCP crystals are triclinic and stable at higher temperatures and lower pH levels in the range of pH 4-5. ADCP have also been shown experimentally to undergo conversion from the unstable states at pH levels greater than 6-7 to the more thermodynamically favourable HA. Furthermore the solubility of ADCP is known to be slightly inferior to that of DCP. This has been confirmed experimentally by the number of calcium and phosphates ions released over a set time in solution. As mentioned previously, the increased release of calcium and phosphate ions can be advantageous as it promotes osseointegration and osteogenesis. Using synthetic production techniques, the size and number of monetite crystals can be controlled relatively easily

by adjusting the concentrations of Ca^{2+} , HPO_4^{2-} and H_2PO_4^- . Current studies have demonstrated the adherence, spread and differentiation of human osteoblast cells on three-dimensional (3-D) printed monetite substrates after periods of 14 and 21 days in culture.

2.6.3 Octacalcium phosphate (OCP)

OCP crystals are structurally triclinic crystals and exist in alternating layers of apatite layers and hydrated layers. OCP is often observed as an intermediary stage in the precipitation of HA and bone-like apatites. It has been suggested and demonstrated experimentally that HA is unable to be formed directly from solution and thus requires an intermediary phase, most often indicated to be OCP. Several synthesis studies have shown OCP to be most stable at a physiological pH and temperature, and have demonstrated the ability of OCP to convert to a bone-like apatite when exposed to slightly more acidic conditions. Furthermore OCP has been established as a precursor for bone mineralization. Subsequently, OCP was suggested as an appropriate implant coating due to its expected conversion to a bone-like apatite in response to the post-surgical acidic conditions consequential to inflammatory responses. In vitro studies have demonstrated OCP to have excellent biocompatibility using mature primary human osteoblast cells, human foetal osteoblast-like cells, rat bone marrow cells, murine fibroblasts, polymorphonuclear neutrophils and peripheral blood mononuclear cells.

2.6.4 Tricalcium phosphate - whitlockite (TCP)

TCP, known mineralogically as whitlockite, commonly exists in two phases: α -TCP and β -TCP. The former phase crystallizes in the monoclinic space group, whilst the latter crystallizes in a rhombohedral space group. Investigations have reported α -TCP to occur when sintered at temperatures

in excess of approximately 1250 ° C, whereas β -TCP has been shown to be the dominant phase at the slightly lower temperatures of 900–1100 ° C. Tricalcium phosphate is often investigated as a biphasic coating in combination with HA, where studies have indicated that the most effective combinations for increased biocompatibility consist of higher HA : TCP ratios. Research has confirmed that this may be due to the greater solubility of TCP when compared with HA, and has further suggested it may be a function of the different porosities of HA and TCP. Alternatively, nominal studies have utilized TCP as a precursor to obtain an OCP structure via hydrolysis in phosphoric acid. Active proliferation of human osteoblast cells, mouse osteoblast cells, rat osteoblast cells and bone marrow stromal cells, has been shown in the presence of TCP-containing structures.

2.6.5 Hydroxyapatite (HA)

HA is the naturally occurring mineral form of calcium apatites and is the major mineral component of bones and teeth. The biological and synthetic stoichiometric structure displays hexagonal symmetry, as was identified in early investigations through X-ray structure analysis. HA has been established experimentally to be thermally stable up to temperatures of 1300 ° C in air, below which phase decomposition is not observed. The existence of non-stoichiometric HA is common more often in the form of fluoride, chloride and carbonate substitutions for hydroxyl groups present in the structure. The biocompatibility of HA has been thoroughly investigated and established, demonstrating proliferation and differentiation of mesenchymal stem cells, and the adhesion of human keratinocyte cell lines. The improved adhesion, proliferation, differentiation and increased alkaline phosphatase activity of primary human osteoblast cells and normal cell growth of human embryonic kidney cell lines in the presence of HA have also been illustrated experimentally. Table 6 [39] shows the typical composition of the inorganic phase of adult human calcified tissues.

Table 6. Typical compositional values of inorganic phase of adult human calcified tissues [39]

Composition	Enamel	Dentin	Bone	Hydroxyapatite
Calcium [wt.%]	36.5	35.1	34.8	39.6
Phosphate(as P)[wt.%]	17.7	16.9	15.2	18.5
Ca/P(molar ratio)	1.63	1.61	1.71	1.67
Sodium [wt.%]	0.5	0.6	0.9	-
Magnesium [wt.%]	0.44	1.23	0.72	-
Potassium [wt.%]	0.08	0.05	0.03	-
Carbonate(as CO_3^{2-})[wt.%]	3.5	5.6	7.4	-
Fluoride [wt.%]	0.01	0.06	0.03	-
Chloride [wt.%]	0.30	0.01	0.13	-
Pyrophosphate (as $\text{P}_2\text{O}_7^{4-}$) [wt.%]	0.022	0.10	0.07	-
Total inorganic [wt.%]	97	70	65	100
Total organic [wt.%]	1.5	20	25	-
Water [wt.%]	1.5	10	10	-
Ignition products (800 °C)	β -TCP+ HA	β -TCP+ HA	HA+ CaO	HA

2.7 Calcium phosphate coating

Calcium hydroxyapatite is highly biocompatible material due to its chemical similarity with inorganic part of the human hard tissue. HA is known as a bioactive ceramic because of its capability to improve osteointegration. Biological reaction to a HA ceramic is strongly dependent on its chemical composition, phase purity and microstructural properties. Besides controlling the stoichiometry of synthetic HA, controlling the crystallinity, porosity, particle shape, surface area and agglomeration characteristics are of the great interest.

For HA production, numerous synthesis method have been used (Table 7). Poor mechanical characteristics make HA material inadequate for application in load-bearing areas. For that reason, the strategies for improving the biocompatibility of metal implants had involved the surface modification by inorganic mineral coatings deposited by different techniques such as pulsed laser deposition, biomimetic process and electrophoretic deposition.

Electrochemical deposition of calcium phosphate bioceramics is an attractive method because of the advantages in the coating fabrication, e.g., low process temperature, the possibility of the deposition onto porous and/or substrate of complex shapes and the simple control of deposit thickness and the morphology. The composition and properties of the coatings deposited electrochemically depend on the typical parameters and conditions, e.g., applied current/voltage, temperature, pH value and the deposition time. The implants based on titanium and its alloys are often coated by osteointegrating and/or osteoconductive materials such as calcium phosphate ceramics. This enhances the implant biocompatibility. The improvement in metal to bone fixation has been proved for the coated implants with respect to uncoated ones. Hence, the calcium phosphate coatings are recognized as biocompatible and able to accelerate the bone ingrowing and adhesion to the surface of implant during the early stages upon implantation.

Table 7. Different technique to deposit HA coatings [38]

Technique	Thickness	Advantages	Disadvantages
Thermal spraying	30–200 μm	High deposition rates; low cost	Line of sight technique; high temperatures induce decomposition; rapid cooling produces amorphous coatings
Sputter coating	0.5–3 μm	Uniform coating thickness on flat substrates; dense coating	Line of sight technique; expensive time consuming; produces amorphous coatings
Pulsed laser deposition	0.05–5 μm	Coating with crystalline and amorphous; coating with dense and porous	Line of sight technique
Dynamic mixing method	0.05–1.3 μm	High adhesive strength	Line of sight technique; expensive; produces amorphous coatings
Dip coating	0.05–0.5 mm	Inexpensive; coatings applied quickly; can coat complex substrates	Requires high sintering temperatures; thermal expansion mismatch
Sol–gel	< 1 μm	Can coat complex shapes; Low processing temperatures; relatively cheap as coatings are very thin	Some processes require controlled atmosphere processing; expensive raw materials
Electrophoretic deposition	0.1–2.0 mm	Uniform coating thickness; rapid deposition rates; can coat complex substrates	Difficult to produce crack-free coatings; requires high sintering temperatures
Biomimetic coating	< 30 μm	Low processing temperatures; can form bonelike apatite; can coat complex shapes; can incorporate bone growth stimulating factors	Time consuming; Requires replenishment and a constant of pH of simulated body fluid
Hot isostatic pressing	0.2–2.0 mm	Produces dense coatings	Cannot coat complex substrates; high temperature required; thermal expansion mismatch; elastic property differences; expensive; removal/interaction of encapsulation material

2.8 Surface wettability

When an implant material is placed inside a human body, among the plethora of events that take place the first and the foremost one is the wetting of the implant material by the physiological fluids. This further controls the adsorption of proteins followed by attachment of cells to the implant surface. Hence surface wettability is considered as an important criterion that can dictate the biocompatibility of the implant material. The three most important factors that affect the wettability of a surface are its chemical composition, microstructural topography, and surface charge. Contact angle measurements are probably the most adopted technique to measure the average wettability of a surface [40].

Contact angle measurements can be carried out by five different techniques known as the (1) static or sessile drop method, (2) Wilhelmy plate method, (3) captive air bubble method, (4) capillary rise method, and (5) tilted drop method. Among the above techniques, static or sessile drop is the most commonly used method. The angle formed between the solid-liquid interface and liquid-vapor interface and which has a vertex where the three interfaces meet is called the contact angle (Fig. 6).

The interfacial tensions of the solid-vapor (γ_{sv}), liquid-vapor (γ_{lv}) and solid-liquid (γ_{sl}) interface, and the contact angle (θ), are related by an equation known as the Young's equation:

$$\gamma_{lv}\cos\theta = \gamma_{sv} - \gamma_{sl}$$

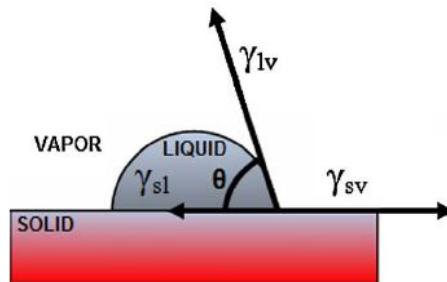


Fig. 6. This schematic illustration of a contact angle formed by a liquid drop at the solid/liquid interface and the liquid/vapor interface.

If the contact angle is high ($>90^\circ$) (Fig. 7(a)) then the surface is considered as a non-wetting or a hydrophobic surface. If the contact angle is small (Fig. 7(b)), then the surface is considered as a wetting or a hydrophilic surface. The energy of the surface (γ_{sv}) which is directly related to the wettability is also a very useful parameter that can strongly affect the biological interaction. But γ_{sv} cannot be directly obtained from the above equation as we have two unknowns γ_{lv} and γ_{sl} . γ_{sv} can only be calculated by solving simultaneous equations with data collected from liquids of different surface tension.

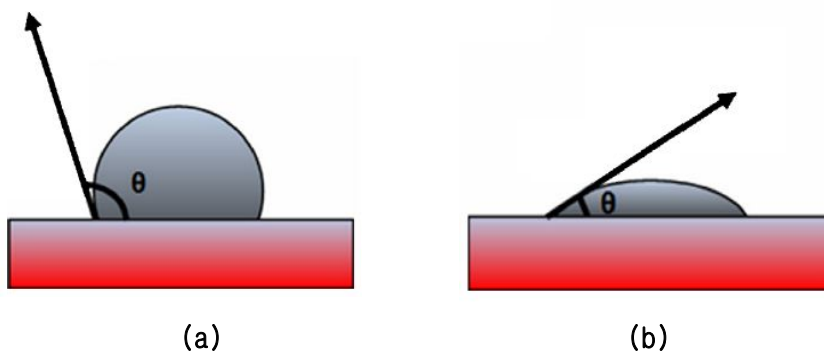


Fig. 7. This schematic illustration of (a) a hydrophobic or non-wetting surface and (b) hydrophilic or wetting surface.

III . MATERIALS AND METHODS

3.1. Alloy Preparation

The Ti-25Nb-xZr alloys, with Zr content ranging from 3, 7 and 15 wt.% were prepared using CP titanium (G&S Titanium, Grade 4, USA), Niobium and Zirconium (Kurt J. Lesker Company, 99.95 wt.% purity, USA). All materials were cleaned by ultrasonic cleaner in acetone, and dried in blowing air. The Ti-25Nb-xZr alloys were fabricated from the component metals, using a vacuum arc-melting furnace (SVT, KOREA) with non-consumable tungsten electrode and water cooled copper hearth under high purity argon atmosphere.

All the ingots were flipped and remelted at least ten times in order to improve their chemical homogeneity. The loss of mass due to sample preparation was calculated to be less than 0.1 %. The ingots of Ti-25Nb-xZr alloys were obtained in the form of rod with about length of 60 mm and diameter of 10 mm, and ingots were approximately 20 g in weight. The ingots of Ti-25Nb-xZr alloys were homogenized in Ar atmosphere at 1000 °C for 24 h followed by quenching into 0 °C water. For manufacture the cylindrical specimens with diameter of 10 mm and thickness of 3 mm, ingots were cut off by diamond wheel cutting system (Accutom-5, Struers, Denmark).

3.2. Phase analysis of Ti-25Nb-xZr alloys

The samples were mechanically polished using various grade of SiC paper and finally using a 0.3 μm diamond paste and then ultrasonically cleaned in acetone and deionized water and finally dried in air. Chemical etching treatment was performed using Keller's reagent with 2 ml HF, 3 ml HCl, 5 ml HNO_3 , 190 ml H_2O . The phase structure and chemical composition of the Ti-25Nb-xZr alloys were identified by using an X-ray diffraction (XRD, X'pert Pro, Philips, Netherlands) and $\text{Cu K}\alpha$ radiation at 40 kV and 30 mA.

XRD patterns were collected in the 2θ ranges from 20 to 90° . Phase was utilized to confirm the samples' chemical composition by matching each characteristic peak with JCPDS-ICDD card. The microstructure of Ti-25Nb-xZr alloys were observed by optical microscope (OM, Olympus, BX60M, Japan), field emission scanning electron microscope (FE-SEM, Hitachi, 4800, Japan) and energy dispersive spectroscopy (EDS, Oxford, England).

3.3. Nanotube formation on Ti-25Nb-xZr alloys

The electrochemical experiments were carried out with a conventional three electrode configuration having a platinum counter electrode and a saturated calomel reference electrode (SCE), respectively. Self-organized TiO_2 were prepared by electrochemical oxidation of the samples in the 1.0 M H_3PO_4 + 0.8 wt.% NaF electrolyte. The operation voltage was 10 V and 2 h (potentiostat 362, EG&G Company, USA)(Table 8).

After electrochemical oxidation, all samples were annealed at 500 °C for 2 h with heating rate of 5 °C/min and cooling rate of 2 °C/min in a furnace. The surface and morphology were observed by a field-emission scanning electron microscope (FE-SEM, Hitachi 4800, Japan) and scanning transmission electron microscope (STEM, JEM-2100F, JEOL, Japan).

Table 8. The conditions of nanotube formation on Ti-25Nb-xZr alloys

Nanotube formation	
Working Equipment	EG&G Co, Model: POTENTIOSTAT 362
Working Electrode	Ti-25Nb-xZr Samples
Reference electrode	Saturated Calomel Electrode
Counter Electrode	Platinum Counter Electrode
Electrolyte	1 M H_3PO_4 + 0.8 wt % NaF
Applied voltage	10 V
Time	2 hr

3.4 HA coating of nanotube formed on Ti-25Nb-xZr alloys by electrochemical deposition method

The electrochemical deposition of calcium phosphate was carried out at 85 °C in modified simulated body fluid (SBF). Before deposition, the specimens were rinsed in deionized water, soaked in 5.0 M NaOH solution at 60 °C for 5 min. The anodization was carried out potentiostat (EG&G Company, Model 2273, USA) and interfaced to a computer using cyclic voltammetry (CV) method.

The pulsing cycle is schematically illustrated in Fig. 8. The electrolyte used for deposition contained 2.5 mM $\text{Ca}(\text{NO}_3)_2$ + 1.5 mM $\text{NH}_4\text{H}_2\text{PO}_4$, 5.0 mM $\text{Ca}(\text{NO}_3)_2$ + 3.0 mM $\text{NH}_4\text{H}_2\text{PO}_4$, respectively (Table 9).

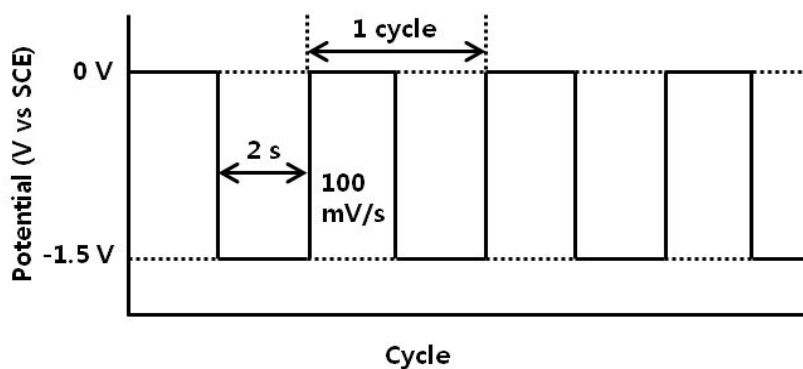


Fig. 8. Process of monitoring voltage versus times during the formation of HA deposition.

Table 9. The condition of electrochemical deposition on nanotubular Ti-25Nb-xZr alloys

Cyclic Voltammetry	
Working Equipment	EG&G Co, Model: PARSTAT 2273
Working Electrode	Ti-25Nb-xZr Samples
Reference Electrode	Saturated Calomel Electrode
Counter Electrode	Platinum Counter Electrode
Electrolyte	Modified SBF Solution
	1) 2.5 mM $\text{Ca}(\text{NO}_3)_2$ + 1.5 mM $\text{NH}_4\text{H}_2\text{PO}_4$
	2) 5.0 mM $\text{Ca}(\text{NO}_3)_2$ + 3.0 mM $\text{NH}_4\text{H}_2\text{PO}_4$
Working Temp.	$85 \pm 1^\circ\text{C}$
Scan rate	0.5 V/s

3.5. Corrosion test for Ti-25Nb-xZr alloys

Corrosion behaviors were performed in a traditional three electrode having the specimen as a working electrode and a high dense carbon counter electrode, respectively. The potential of the working electrode was measured against a saturated calomel electrode (SCE) and all specimen potentials were referenced to this electrode.

The corrosion properties of the specimens were examined by a potentiodynamic test (potential range from -1500 to 2000 mV) at scan rate of 1.67 mV/s in 0.9 % NaCl solution at 36.5 ± 1 °C with neutral pH value. (PARSTAT 2273, EG&G Company, USA). Using an automatic data acquisition system, the potentiodynamic polarization curves were plotted and both corrosion rate and potential were estimated by Tafel plots by using both anodic and cathodic branches. The condition of electrochemical corrosion test were shown in Table 10.

Table 10. The conditions of electrochemical corrosion test on Ti-25Nb-xZr alloys

Potentiodynamic test	
Working Equipment	EG&G Co, Model: PARSTAT 2273
Working Electrode	Ti-25Nb-xZr Samples
Reference Electrode	Saturated Calomel Electrode
Counter Electrode	High Dense Carbon
Electrolyte	0.9% NaCl
Working Temp.	36.5±1°C
Gas Purging	Ar gas, 10min
Scan rate	1.67 mV/s
Scan Definition	-1500 ~ +2000mV

IV. RESULTS AND DISCUSSION

4.1. Microstructures and XRD analysis of Ti-25Nb-xZr alloys

Ti-25Nb-xZr alloys were analyzed optical microscope, field emission scanning electron microscope and x-ray diffraction. Fig. 9 and 10 present the surface view OM and FE-SEM images of Ti-25Nb-xZr alloys with different Zr content (3, 7 and 15 wt.%), respectively. Microstructures of Ti-25Nb-xZr alloys were changed needle-like to equi-axed with Zr content and both β and α'' phases are examined all specimen by XRD. The α'' phase shows a kind of acicular structure in equi-axed β grains, as shown in Fig. 9(a).

Fig. 9(b) and (c) are composed of equi-axed β phase owing to the increase of Zr content which restrains martensitic transformation in quenching process. Fig. 11 shows the peaks on the XRD patterns of Ti-25Nb-xZr alloys. The XRD pattern identification was confirmed by analyzing from the JCPDS-ICDD card.

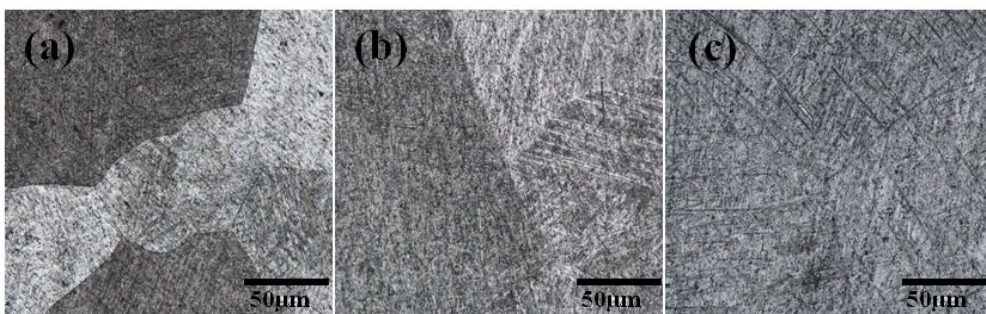


Fig. 9. OM images of Ti-25Nb-xZr alloys
 (a) Ti-25Nb-3Zr, (b) Ti-25Nb-7Zr and (c) Ti-25Nb-15Zr.

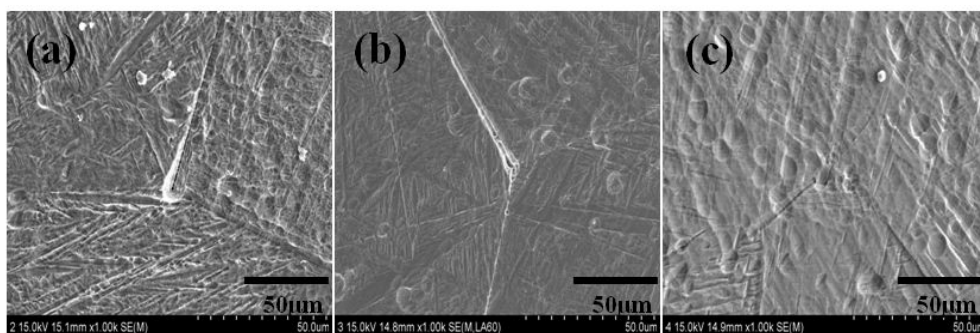


Fig. 10. FE-SEM images of Ti-25Nb-xZr alloys
 (a) Ti-25Nb-3Zr, (b) Ti-25Nb-7Zr and (c) Ti-25Nb-15Zr.

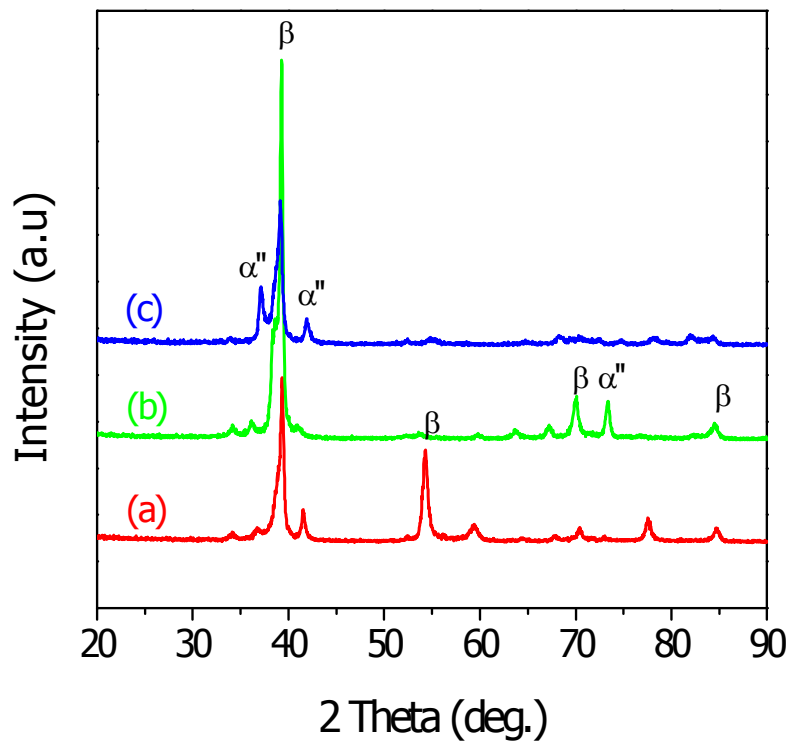


Fig. 11. XRD patterns of Ti-25Nb-xZr alloys
(a) Ti-25Nb-3Zr, (b) Ti-25Nb-7Zr and (c) Ti-25Nb-15Zr.

4.2. The nanotube formed of Ti-25Nb-xZr alloys

Fig. 12 shows the surface morphology of top view, cross-section and bottom view of nanotube layers formed on Ti-25Nb-xZr alloys. Fig. 12(a, b and c) provides a global view of the nanotube arrays. From the magnification, the nanotubes were found to be slightly squeezed into an elliptic shape. Fig. 12(a, b and c), it can be estimated that the nanotubes have the average diameter of about 100 nm. These dimensions were obtained under the conditions of 10 V and 2 h anodic oxidation time in the electrolyte containing 1.0 M H_3PO_4 + 0.8 wt.% NaF. If the voltage and time for the oxidation or the electrolyte composition were changed, the dimensions of the nanotube could be changed, as indicated earlier in literature [41,42].

Fig. 12(a-1, b-1 and c-1) shows the cross-section of nanotube layers. The addition of more Zr to the Ti-25Nb-xZr alloys composition can cause the nanotube structure to have a more highly ordered morphology with increased length. In order for the bottom images to present the more detailed information, they were acquired from mechanically scratched samples which had caused some pieces to flake off and lie upside down. As more clearly shown in the bottom surface images of Fig. 12(a-2, b-2, and c-2), the nanotube layer on the Ti-25Nb-xZr alloys consisted of two different structures with large tubes and small tubes. The diameters of the large tubes ranged from approximately 180 nm to 220 nm, and the diameters of the small tubes ranged from approximately 80 nm to 110 nm. These different nanotube structures were created by the incorporation of Zr in the Ti-25Nb-xZr alloys. Also, it can be seen that increasing the Zr concentration in the Ti-25Nb-xZr alloys caused incremental changes in tube diameter and shapes from an irregular surface on the Ti-25Nb-3Zr alloy in Fig. 12(a-2) to highly ordered surfaces on the Ti-25Nb-7Zr and Ti-25Nb-15Zr alloys in Fig. 12(b-2, c-2).

For a more precise analysis, cross-sections of the nanotube structure on the Ti-25Nb-15Zr alloy were examined by STEM. Fig. 13 shows bright-field images with diffraction patterns and compositions from EDS analysis obtained by STEM for the nanotube structures on the Ti-25Nb-15Zr alloy. As shown in Fig. 13, a distinct interface existed between the nanotubes and the barrier

oxide layer. As previously shown in Fig. 12, 13 clearly reveals in cross-section the two different morphologies of the nanotube structure with large tubes and small tubes. The two sizes observed for the diameters of the nanotubes may be ascribed to the difference in growth rate and dissolution rate during the formation of each group of nanotubes [43]. Additionally, bamboo-like rings are evident in the nanotube structure shown in Fig. 13. These bamboo-like rings are attributed to the effect of F⁻ ions on the local tube dissolution and formation processes. For these phenomena, it is suggested that the first nanotube nuclei on the metal oxide film were nucleated and grew due to differences in the ionization potentials of Ti, Nb and Zr in the alloy compositions [44].

From the SAD pattern in Fig. 13, it can be seen that all nanotube surfaces on the Ti-25Nb-15Zr alloy have featureless patterns that correspond to an amorphous phase which has not undergone crystallization. It is assumed that the different sizes of nanotubes formed due to the different dissolution rates of the oxide film components on the Ti-25Nb-xZr alloys caused by the fluoride ions. Fig. 13 by EDS analysis, oxygen was detected in near matrix (part 4), whereas, in nanotube (part 1, 3 and 6) barrier layer (part 2, 5), oxygen peaks increased predominantly compared to peaks of oxygen in near matrix (part 4). Also the detection of Ti, Nb and Zr oxides consisted of Ti, Nb and Zr in the nanotube confirmed oxide films from the XPS analysis [44].

Fig. 14 shows XRD patterns of nanotube formed on Ti-25Nb-xZr alloys. The amorphous structure of nanotube arrays was changed to anatase at 450 °C inside the tube wall and was entirely changed to rutile at 600 °C by annealing [45]. To crystallize the nanotube surface, all samples were annealed at 500 °C for 2 h. After this heat treatment, the peaks for TiO₂ (rutile and anatase) were predominant.

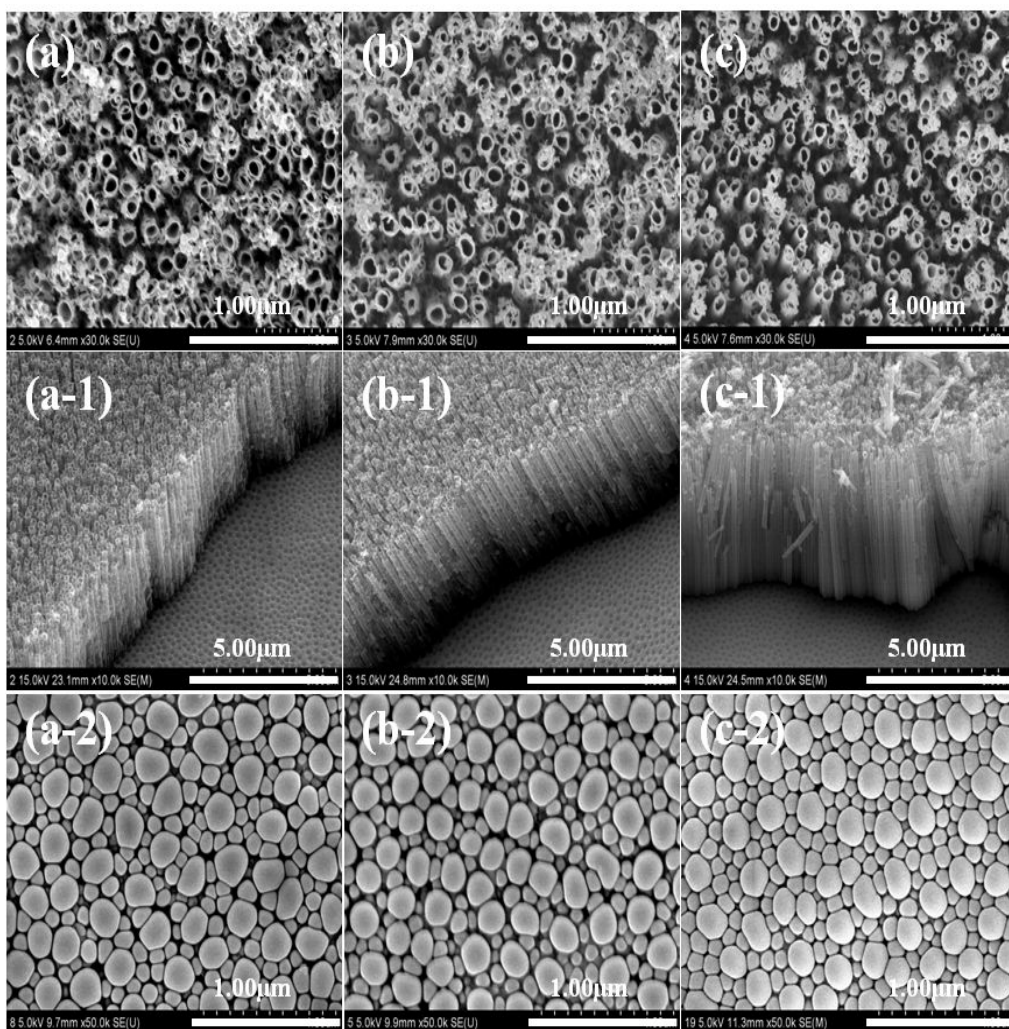


Fig. 12 FE-SEM images of nanotube formed on Ti-25Nb-xZr alloys:
top view, cross-section and bottom view
(a) Ti-25Nb-3Zr, (b) Ti-25Nb-7Zr and (c) Ti-25Nb-15Zr.

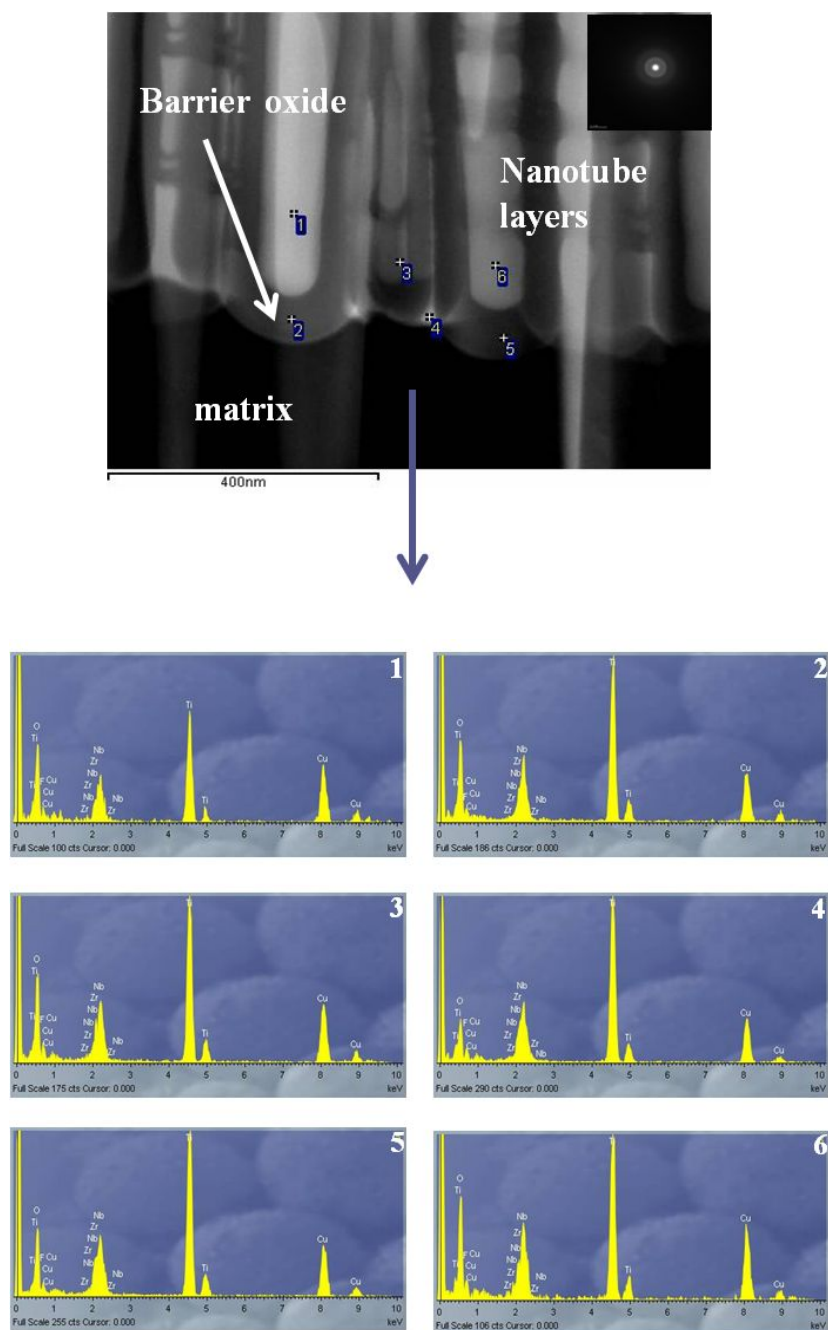


Fig. 13 Bright-field STEM images, diffraction patterns, and EDS peaks for cross-sectioned nanotube surfaces on Ti-25Nb-15Zr alloy.

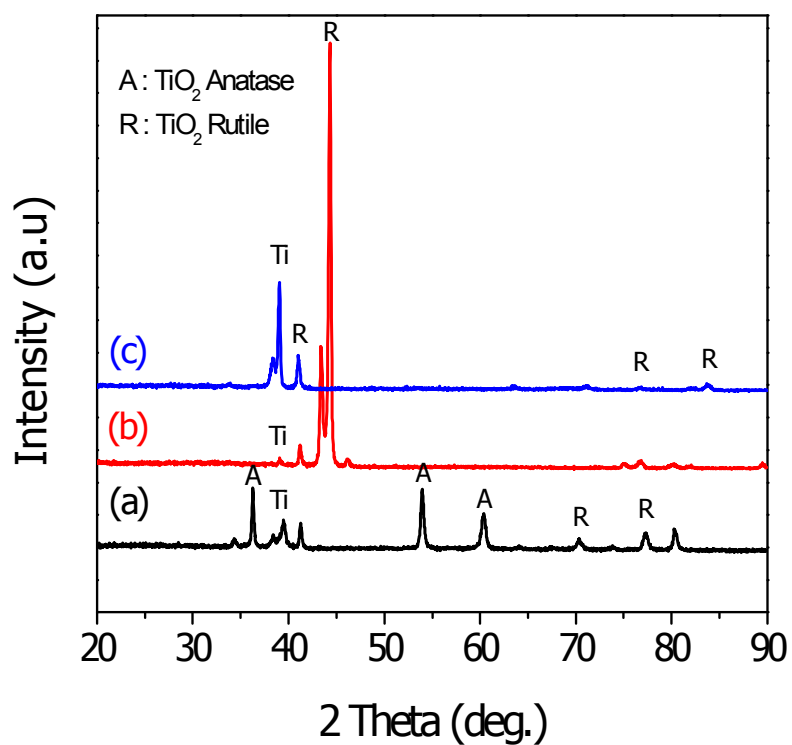


Fig. 14. XRD patterns of nanotube formed on Ti-25Nb-xZr alloys
(a) Ti-25Nb-3Zr, (b) Ti-25Nb-7Zr and (c) Ti-25Nb-15Zr.

4.3. Electrochemical characteristics of Ti-25Nb-xZr alloys with surface treatment

Fig. 15 and 16 shows the polarization curves of Ti-25Nb-xZr alloys after potentiodynamic test in 0.9 % NaCl solution at 36.5 ± 1 °C. The results for E_{corr} (corrosion current potential), I_{corr} (corrosion current density), $I_{300\text{mV}}$ (corrosion current density of oral environment at 300 mV) and I_{pp} (current density of primary passivation) from the polarization curves are given to Table 11. These values were obtained from the polarization curves and Tafel plots using both the cathodic and anodic branches of the curves, respectively.

Polarization curves were shifted to left side with increasing Zr content. From the polarization curves in Fig. 15, Ti-25Nb-15Zr alloy observed the highest value of corrosion potential compared to Ti-25Nb-3Zr alloy. It is confirmed that the thick ZrO_2 film is formed on the surface with addition of Zr element to Ti-25Nb system. The potentiodynamic test of Ti-25Nb-xZr alloys indicated that Zr content significantly increased the electrochemical performance and it can be an important factor for the improvement of osseointegration [7].

Fig. 16 shows nanotube formed on Ti-25Nb-xZr alloys after potentiodynamic test in 0.9 % NaCl solution at 36.5 ± 1 °C. Due to large surface area of nanotube, it can be seen that E_{corr} is lower and I_{corr} is higher for the Ti-25Nb-xZr alloys with nanotube surface than those of non-treated surface. However, the passive region of nanotube surface is more stable and wider than non-treated surface, suggesting that the mixed TiO_2 , Nb_2O_5 and ZrO_2 film is stable [6].

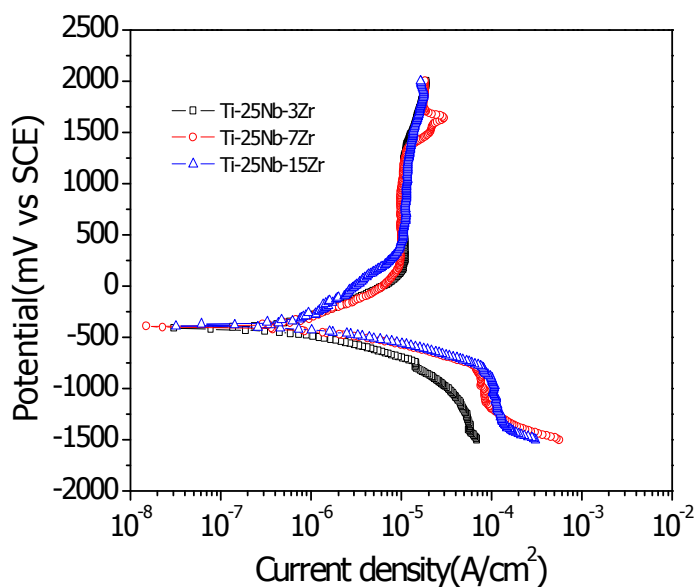


Fig. 15. Polarization curve of Ti-25Nb-xZr alloys after potentiodynamic test in 0.9 % NaCl solution at 36.5 ± 1 °C.

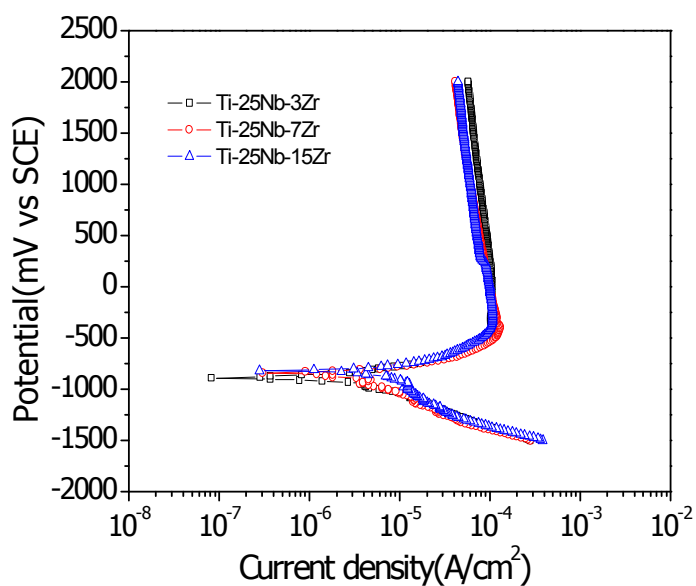


Fig. 16. Polarization curve of nanotube formed on Ti-25Nb-xZr alloys after potentiodynamic test in 0.9 % NaCl solution at 36.5 ± 1 °C.

Table 11. Electrochemical parameter of non-treated and nanotube formed Ti-25Nb-xZr alloys from polarization curves: Corrosion current density (I_{corr}), current density at 300mV(I_{300mV}), corrosion current potential (E_{corr}) and passivation current density(I_{pass})

Sample		$E_{corr}(mV)$	$I_{corr}(A/cm^2)$	$I_{300mV}(A/cm^2)$	$I_{pp}(A/cm^2)$	βa (mV/dec)	βc (mV/dec)
Alloys	3Zr	-412	6.80×10^{-6}	1.12×10^{-5}	9.86×10^{-6}	432	237
	7Zr	-395	8.05×10^{-6}	9.85×10^{-6}	8.68×10^{-6}	457	198
	15Zr	-380	1.12×10^{-6}	1.06×10^{-5}	8.26×10^{-6}	501	178
Nanotube Formed	3Zr	-890	1.60×10^{-6}	9.93×10^{-5}	1.02×10^{-4}	175	190
	7Zr	-838	5.07×10^{-6}	8.55×10^{-5}	1.24×10^{-4}	219	592
	15Zr	-821	8.74×10^{-6}	7.84×10^{-5}	9.63×10^{-5}	344	643

4.4. HA coating of nanotube formed on Ti-25Nb-xZr alloys

Fig. 17 shows FE-SEM micrographs of Hydroxyapatite coating on nanotube formed Ti-25Nb-15Zr alloy in various modified SBF electrolyte with 5, 10, 30 cycles of potential. Fig. 17(a and b) shows that nanotube structures were gathered each other. Needle-like precipitates were observed at modified SBF (Fig. 17(a-1 and b-1)) and plate-like precipitates also observed (Fig. 17(a-2 and b-2)). As the modified SBF electrolyte concentration is increased, needle-like deposits transferred to the plate-like structure. From the surface morphology, width size of Hydroxyapatite increased with increasing the electrolyte concentration.

Fig. 18 shows XRD patterns of the Hydroxyapatite coating on nanotube formed Ti-25Nb-15Zr alloy in various modified SBF electrolyte concentrations with 30 cycles of potential. The diffraction peaks of HA were observed in the all specimens. The peaks are clearly indicative of HA were seen throughout the pattern with 2θ values that correspond closely to those observed in the JCPDS-ICDD card. The intensities of the peaks of HA increased with the increasing electrolyte concentrations and those of HA were the highest at 5 mM Ca-P solution.

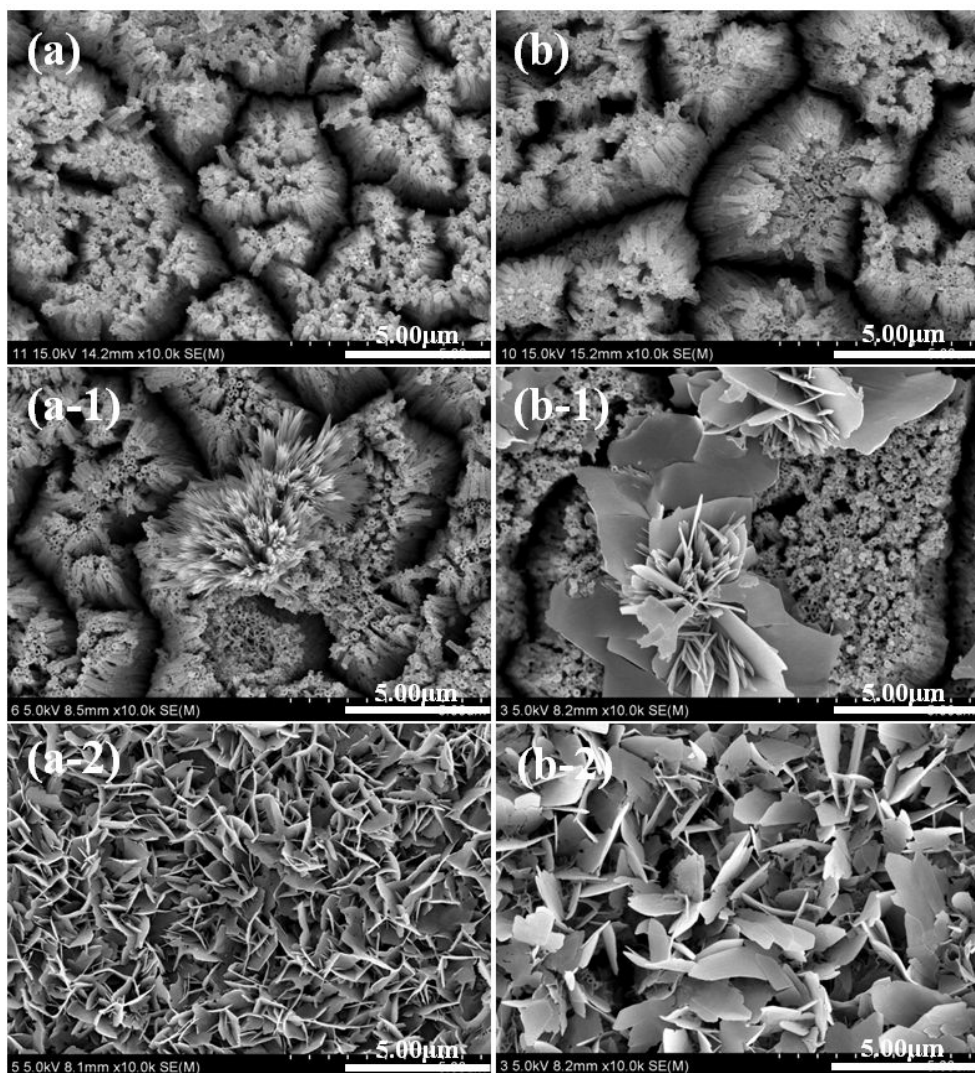


Fig. 17. FE-SEM micrographs of Hydroxyapatite coating by 2.5 mM $\text{Ca}(\text{NO}_3)_2$ + 1.5 mM $\text{NH}_4\text{H}_2\text{PO}_4$ electrolyte with 5, 10, 30 cycles of potential on nanotube formed Ti-25Nb-15Zr alloy(a, a-1 and a-2) and 5.0 mM $\text{Ca}(\text{NO}_3)_2$ + 3.0 mM $\text{NH}_4\text{H}_2\text{PO}_4$ electrolyte with 5, 10, 30 cycles of potential on nanotube formed Ti-25Nb-15Zr alloy(b, b-1 and b-2).

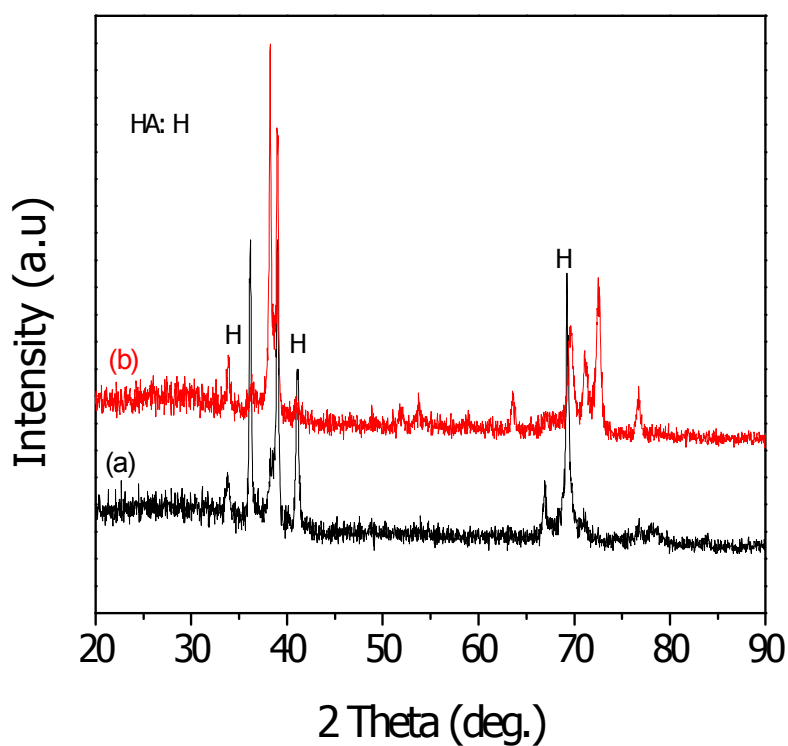


Fig. 18. XRD patterns of Hydroxyapatite coating on nanotube formed Ti-25Nb-15Zr alloy
(a) 2.5 mM Ca-P solution (b) 5.0 mM Ca-P solution.

4.5. Surface wettability test of Ti-25Nb-xZr alloys

Contact angle behavior evaluated on Ti-25Nb-xZr alloys which have pronounced topological features and increased surface areas. Fig. 19 shows snap shot of contact angle as an indication of surface wettability and biocompatibility with different surface treatment. Also, Fig. 20 shows the contact angles values of water droplets measured on the different surface treatment.

In Fig. 20, the contact angle of non-treated alloys are average $63 \pm 3^\circ$ and nanotube formed alloys show the improved the wettability and reduce the contact angle significantly (average $24 \pm 3^\circ$) due to nanotube arrays provide the liquid to penetrate and thus lower the contact angle, which created a surface more hydrophilic surface. Fig. 19, 5.0 mM Ca-P show the lower value of average $2 \pm 3^\circ$ compare with 2.5 mM Ca-P (average $15 \pm 3^\circ$). In general, lower contact angle also leads to higher surface energy.

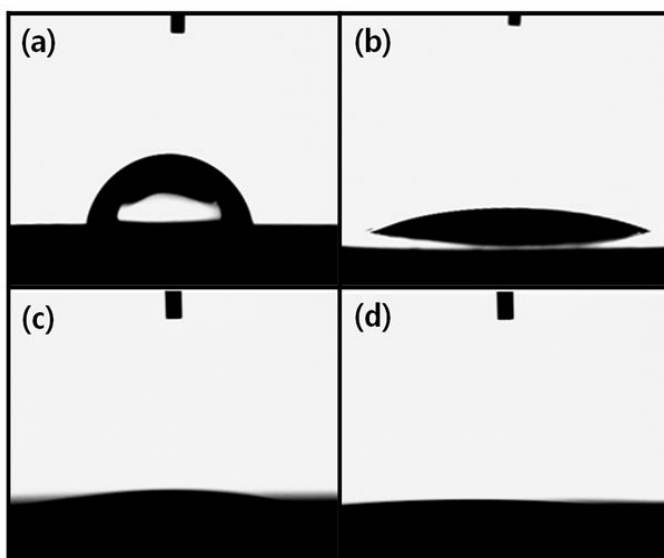


Fig. 19. Snap shot of contact angles on the different surface treatment
 (a) non-treated alloys (b) nanotube formed alloys
 (c) 2.5 mM Ca-P solution alloys and (d) 5.0 mM Ca-P solution alloys.

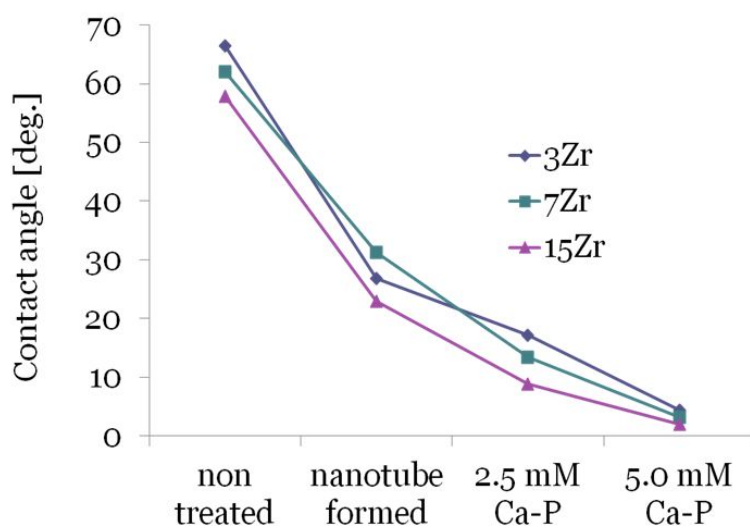


Fig. 20. Contact angles values of water droplets measured on the different surface treatment.

V. CONCLUSIONS

In this study, the hydroxyapatite film coating on the nanotubular Ti-25Nb-xZr alloys by electrochemical deposition method, have been investigated as follows:

1. Microstructures of Ti-25Nb-xZr alloys were shown needle-like structure to equi-axed structure as Zr content increased.
2. The XRD patterns of the nanotube formed on Ti-25Nb-xZr alloys showed that the samples annealed at 500 °C contained anatase phase and rutile phase.
3. Polarization curves were shifted to left side with increasing Zr content. It is confirmed that the thick ZrO_2 film is formed on the surface. Nanotube formed on Ti-25Nb-xZr alloys was shown lower E_{corr} and higher I_{corr} than those of non-treated surface. However, the passive region of nanotube surface is more stable and wider than non-treated surface.
4. Nanotube formed on Ti-25Nb-xZr alloys show two scale of nanotube structure. The diameters of the large tubes ranged from approximately 180 nm to 220 nm, and the small tubes ranged from approximately 80 nm to 110 nm. These different nanotube structures were created by the incorporation of Zr content.
5. Nanotube formed on Ti-25Nb-xZr alloys observed the low contact angle, good wettability and biocompatibility. Especially, Hydroxyapatite coating of nanotube formed on Ti-25Nb-xZr alloys in 5.0 mM Ca-P surface shows a hydrophilic behavior (average $2 \pm 3^\circ$), that is complete spreading

of water on the entire.

6. Nanotube formed pores were covered with Hydroxyapatite layer. It is confirmed that the amounts and morphology of deposits were influenced by the electrolyte concentration and current density. Depending on the modified SBF concentration, Hydroxyapatite was formed with needle-like and plate shape of nanotube formed on Ti-25Nb-xZr alloys.

In conclusion, It is clear that Hydroxyapatite coating of nanotube formed on Ti-25Nb-xZr alloys have arrays of nano phase structure by electrochemical deposition method. Hydroxyapatite was precipitated densely in the nanotube pore and connected with each other in the TiO_2 layer. Nanotubes ensured nucleation of the hydroxyapatite within the nanotubes and improved the bond strength, high corrosion resistance and biocompatibility.

– Reference –

1. M. Niinomi, *Metall. Mater. Trans.* 33A (2002) 477.
2. M. Semlitsch, *Titan* 2 (1986) 721-740.
3. J.A. Davidson, A.K. Mishra, P. Kovacks, R.A. Poggie, *Bio-Med. Mater. Eng.* 4 (1994) 231-243.
4. S. Rao, T. Ushida, T. Tateishi, Y. Okazaki, S. Asao, *Bio-Med. Mater. Eng.* 6 (1996) 79-86.
5. W.F. Ho, C.P. Ju, H. Chern Lin, *Biomaterials* 20 (1999) 2115-2122.
6. M. Niinomi, *Mater. Sci. Eng.* A243 (1998) 231-236.
7. J.A. Davidson, P. Kovacks, U.S. Patent no. 5, 169, 597, December 8, 1992.
8. Y. Li, C. Wang, T. Haung, C. Chen, C. Kao, S. Ding, *Surf. Coat. Technol.* 197 (2005) 367.
9. L. Guo, H. Li, *Surf. Coat. Technol.* 185 (2004) 268.
10. G.K. Mor, O.K. Varghese, M. Paulose, N. Mukherjee, C.A. Grimes, J. *Mater. Res.* 18 (2003) 2588.
11. R. Chu, J. Yan, S. Lian, Y. Wang, F. Yan, D. Chen, *Solid State Commun.* 130 (2004) 789.
12. Y. Lu, M. Li, S. Li, Z. Wang, R. Zhu, *Biomaterials* 25 (2004) 4393.
13. R.R. Kumar, M. Wang, *Mater. Lett.* 55 (2002) 133.
14. J. Weng, Q. Liu, J.G.C. Wolke, X. Zhang, K. de Groot, *Biomaterials* 18 (1997) 1027.
15. M. Shirkhanzadeh, *J. Mater. Sci. Lett.* 10 (1991) 1415.
16. S. Ban, S. Maruno, *Biomaterials* 16 (1995) 977.
17. R. Boyer, G. Welsh, E.W. Collings, *Materials Properties Handbook-Titanium Alloys*, ASM International, Materials Park, OH, 1994.
18. W. Smith, *Structure and Properties of Engineering Alloys*, 2nd ed., McGraw-Hill, New York, 1993.
19. E.W. Collings, *American Society for Metals*, 1984.
20. D. Eylon, *J. Met.* (1984) 55.
21. R. Pederson, *Licentiate Thesis*, Lulea University of Technology, 2002.
22. S.B. Maslennkov, E.A. Maslennkova, *Steels and Alloys at High Temperatures*, Metallurgy Press, Moscow, (1991) 465.

23. A. Balevski, Materials Science, Tehnica Press, Sofia, (1972) 361.
24. Titanium-technical Guide, ASM International, Metals Park, OH, 1988.
25. S. Seagle, H. Kessler, ASM Battelle Memorial Institute, Columbus, 1968.
26. D. Salmon, Low Temperature Data Handbook, Titanium and Titanium Alloys, 1979.
27. J. Destefani, ASM Handbook, vol. 2, ASM International, (1990) 586.
28. R. Wood, Titanium Alloys Handbook, Metals and Ceramics Information Center, Battelle, 1972, Publication number MCIC-HB-02.
29. T. Nishimura, T. Mizoguchi, Y. Itoh, Kobe Res. Dev. 34 (1984) 63.
30. W. Lee Williams, Proceedings of the International Conference, Pergamon Press, London, 1970.
31. Y. Tamura, A. Yokoyama, F. Watari, M. Uo, T. Kawasaki, Mater. Trans. 43 (12) (2002) 3043.
32. X. Nie, A. Leyland, A. Matthews, Surf. Coat. Technol. 125 (2000) 407.
33. Y. Fu, N.L. Loh, A.W. Batchelor, D. Liu, X. Zhu, J. He, K. Xu, Surf. Coat. Technol. 106 (1998) 193.
34. A.C. Fraker, A.W. Ruff, P. Sung, A.C. Van Orden, K.M. Speck, in: H.A. Luckey, F. Kubli(Eds.), ASTM Special Technical Publication, (1983) 206.
35. U. Diebold, Surf. Sci. Rep. 48 (2003) 53.
36. Prakasam, H.E. et al, J. Phys. Chem. C 111, (2007) 7235-7241.
37. G.K. Mor, O.K. Varghese, M. Paulose, K. Shankar, C.A. Grimes, Sol. Energy Mater. Sol. Cells 90 (2006) 2011.
38. FCM Driessens, Monographs in oral science 10 Karger, 1982.
39. Dorozhkin SV, Eppler M, Angew Chem Int Ed 2002; 41: 3130-46.
40. T. Yasuda, T. Okuno, Langmuir 10 (1994) 2435-2439.
41. C.C. Chen, J.S. Lin, E.W. Diau, T.Z. Liu, Appl. Phys. A 92 (2008) 615.
42. Z. Zhang, M.F. Hossain, T. Takahashi, Int. J. Hydrogen Energy 35 (2010) 8528.
43. H. Tsuchiya, J.M. Macak, A. Ghicov, Y.C. Tang, S. Fujimoto, M. Niinomi, T. Noda, P. Schmuki, Electrochem, Acta, 52, (2006) 94.
44. W. M. Haynes, D. R. Lide, CRC handbook of chemistry and physics, CRC Press, New York, (2010) 196.
45. Neupane MP, Park IS, Lee MH, Bae TS, Watari F, Bio-Med. Mater. Eng. 19 (2009) 77-83.

감사의 글

대학원 생활이 어느덧 2년이 되었습니다. 졸업논문의 마무리와 함께 감사의 글을 남기려하니 많은 분들이 생각나네요. 인생에서 또 한번의 값진 인연이 되어주신 분들께 짧게나마 감사의 마음을 전합니다.

부족한 저에게 항상 격려와 가르침을 주셨던 지도교수 이현규 교수님의 은혜에 깊이 감사드립니다. 연구와 강의로 바쁘신 가운데 논문을 지켜봐주신 박진성 교수님, 세심한 부분까지 지적과 수정을 해주신 강현철 교수님께 깊은 감사의 뜻을 전합니다. 생체 재료에 대한 조언과 가르침을 주신 최한철 교수님께도 깊은 감사를 드립니다. 곧 시애틀로 가셔서 연구하시게 될 열정으로 가득차신 박창선 교수님, 디펜스를 잘 마칠 수 있게 배려해주셨던 오용택 교수님께도 깊은 감사를 드리고, 뜻밖의 인연으로 뵈게 된 박영석 교수님께도 감사의 마음을 표하고 싶습니다. 늘 건강하시고 행복하세요.

대학원 공부를 권유해주셨던 박수정 박사님, 김비룡 박사님께도 깊은 감사의 마음을 전합니다. 덕분에 대학원생활을 잘 마무리 할 수 있었습니다. 끊임없는 조언과 부족한 부분을 채워주셨던 이강 박사님, 정말 감사합니다. 조교로 1년 반 동안 생활하게 된 X-선 분석실, 늘 배려해주시고 아낌없이 조언해주신 김종균 박사님과 윤지성 쌤한테도 감사하고 고맙다는 말 전하고 싶습니다. 나의 학부동기들아, 앞으로 1년 남았다. 열심히 해서 꼭 좋은 결과 얻기를 바란다. 항상 고마운 은주, 너에겐 고마운 마음을 이루 표현하기 어렵다. 좋은 사람만나서 알콩달콩 연애하기를 기도할게! 언제나 도와주고 격려를 아끼지 않았던 건웅오빠, 신영오빠. 고맙고 또 고맙네. 항상 응원해 준 혁아, 너의 숨씨 기대하겠어! 여러분의 앞날에 무한한 영광과 발전이 함께 하시길 바랍니다.

내 삶의 공기와 같은 존재, 우리 가족들. 늘 저를 믿고 응원해주시고 아낌없이 사랑 해주시는 부모님께 마음 깊이 감사드립니다. 든든한 동생 상현아, 늘 뭐든지 누나와 함께 고민해줘서 고마워. 누나 널 믿는다! 군복무중인 보고 싶은 막내 재명아, 많이 성숙해져 어른스러워지는 너의 모습을 보면서 참 뿌듯했단다. 조금만 더 힘을 내자!

내 친구들, 특히. 사론에게 넘치는 고마운 마음을 전한다. 항상 관심과 격려를 해준 슬기, 고민을 나눠주고 기쁨을 함께해 준 세미에게도 고맙다고 전하고 싶다. 수연아, 얼마 전에 태어난 너의 아기가 건강하고 씩씩한 녀석으로 자라나길 기도할게! 안 적으면 많이 섭섭해 할 봉동식구들, 지애, 혜지 그리고 세인에게 고맙다고 말하고 싶고, 조만간에 함께할 호주식구들, 태오, 지연, 도형, 문열, 지혜에게도 고마운 마음을 전한다. Hiroko! ごけっこん、おめでとうございます。

2012년 12월 눈 내리는 어느 날에
소민올림